

Open Archive TOULOUSE Archive Ouverte (OATAO)
OATAO is an open access repository that collects the work of Toulouse researchers and makes it freely available over the web where possible.

This is an author-deposited version published in : http://oatao.univ-toulouse.fr/
Eprints ID : 11778

To link to this article : DOI:10.1016/j.jcp.2013.08.023
URL : http://dx.doi.org/10.1016/j.jcp.2013.08.023

To cite this version : Vincent, Stéphane and Brändle de Motta, Jorge César and Sarthou, Arthur and Estivalezes, Jean-Luc and Simonin, Olivier and Climent, Eric *A Lagrangian VOF tensorial penalty method for the DNS of resolved particle-laden flows.* (2014) Journal of Computational Physics, vol. 256 . pp. 582-614. ISSN 0021-9991

Any correspondance concerning this service should be sent to the repository administrator: staff-oatao@listes-diff.inp-toulouse.fr

A Lagrangian VOF tensorial penalty method for the DNS of resolved particle-laden flows

Stéphane Vincent [a,*], Jorge César Brändle de Motta [b,c], Arthur Sarthou [a,c], Jean-Luc Estivalezes [b,c], Olivier Simonin [c], Eric Climent [c]

[a] Université de Bordeaux, Institut de Mécanique et Ingénierie (I2M) – UMR 5295, F-33400 Talence, France
[b] ONERA, The French Aerospace Lab, 2, avenue Edouard Belin, 31055 Toulouse, France
[c] Université de Toulouse, Institut de Mécanique des Fluides de Toulouse, IMFT, UMR 5502, Allée Camille Soula, 31400 Toulouse, France

Keywords:
DNS of particle flows
Resolved scale particles
Viscous penalty method
Lagrangian VOF
Fluidized beds
Collision and lubrication models

A B S T R A C T

The direct numerical simulation of particle flows is investigated by a Lagrangian VOF approach and penalty methods of second order convergence in space for incompressible flows interacting with resolved particles on a fixed structured grid. A specific Eulerian volume of fluid method is developed with a Lagrangian tracking of the phase function while the solid and divergence free constraints are ensured implicitly in the motion equations thanks to fictitious domains formulations, adaptive augmented Lagrangian approaches and viscous penalty methods. A specific strategy for handling particle collisions and lubrication effects is also presented. Various dilute particle laden flows are considered for validating the models and numerical methods. Convergence studies are proposed for estimating the time and space convergence orders of the global DNS approach. Finally, two dense particle laden flows are simulated, namely the flow across a fixed array of cylinders and the fluidization of 2133 particles in a vertical pipe. The numerical solutions are compared to existing theoretical and experimental results with success.

1. Introduction

Interactions between solid particles and a surrounding viscous fluid occurs in many environmental and industrial applications such as combustion devices [1], oil cracking [2], fluidized beds in coal stations and nuclear reactors [3], erosion of sediments on beaches [4] or hygiene and safety [5]. In all these applications, the interaction between the particles and the fluid flow is associated to unsteadiness or turbulence in a complex and not yet well understood manner concerning the drag laws of particles [6] or wall laws of the particulate flow as soon as the particle density is significant. On the one hand, leading simulations at the reactor scale for fluidized beds or combustion chambers require the implementation of macroscopic Eulerian–Eulerian models [7,8] in which a separation scale is assumed between the particle and the flow scales. These models require drag laws and wall boundary conditions for the flow and the particles which are not yet well posed for dense particle flows. On the other hand, the Direct Numerical Simulation (DNS) of resolved particle flows, for which the grid size is smaller than the particle diameter, are generally restricted to academic configurations including a maximum of thousand of particles. The present work aims at presenting a numerical modeling strategy for the DNS of dense particle flows, validated on various physical test cases including particle–particle and particle–wall interactions or particle settling as well as numerical convergence studies. This DNS particle flow solver will be devoted to simulating the interaction between unsteady or turbulent flows and dense whole of particles to understand the particle response to turbulent flows and

* Corresponding author.
E-mail address: vincent@enscbp.fr (S. Vincent).

the modification of turbulence due to the presence of the particles [9]. The DNS tool will allow to extract Lagrangian and Eulerian quantities such as the Lagrangian time scale of the particles, their drag laws or the autodiffusion coefficients [10].

Simulating unsteady particle-laden flows where particle and fluid have the same characteristic scales, *i.e.* resolved scale particle flows, is the scope of the present work. The Direct Point Simulation (DPS) approaches based on a Lagrangian modeling of the particles does not remain valid for that purpose [11–13]. The field of numerical methods devoted to the simulation of particulate flows involving finite size particles was widely developed the last 20 years concerning the study of the flow over a small number of fixed or moving particle [14–19] or a fixed arrangement of spheres [20]. All the previously mentioned works were developed on fixed grids. The unstructured Arbitrary Eulerian–Lagrangian (ALE) grid simulations were developed for particle flows in the 90's by Hu et al. [14] concerning two-dimensional flows involving two particles. The works of Maury [21] with the ALE method are also to be noticed concerning the flow of 1000 non-spherical particles in a two-dimensional biperiodic domain. With the same type of approach, two-dimensional ALE simulations of particle motions involving 320 cylinders in a channel have been studied by Cho et al. [22]. However, few of the existing research works have been extended to the simulation of particle flows involving thousand of particles in three dimensions. The work of Hu et al. concerning three-dimensional ALE simulations of the segregation of 90 particles in a vertical channel are among the most advanced results with adapted unstructured grids [23]. A majority of the particulate flow simulations were carried out on structured grids to avoid the complexity of managing an evolving adapted mesh. Among them, the most relevant existing works concern the distributed Lagrangian multiplier (DLM) method of Glowinski and co-workers [24], the Physalis CFD code of Zhang and Prosperetti [25], the Immersed Boundary (IB) with direct forcing approach proposed by Uhlmann [26,27], the lattice Boltzmann scheme [28,29], the modified version of Uhlmann IB method published by Lucci et al. [30,31] and the viscous penalty techniques of Ritz and Caltagirone [32] and Randrianarivelo et al. [33,34].

To begin with, the DLM method [24] uses a variational formulation of the Navier–Stokes equations on a fixed grid and the Newton–Euler equations in the solid medium to model the particulate flow. On the interface between the particles and the fluid, Lagrange multipliers are integrated in the variational formulation to satisfy the rigid body motion inside the moving bodies. The force resulting from the interaction between particles is treated by an explicit modification of the particle positions after advection in order to avoid particle overlapping. A short range repulsive force is added in the right hand side of the Newton–Euler equations which is decreasing according to the distance between the center of mass of two particles [24]. The DLM method was utilized to simulate with success the fluidization of 1024 spheres in a square shape tank [35]. As for the Physalis approach [25], fixed grids for the flow solving are combined with analytical Stokes solutions in the vicinity of the particles in order to model the fluid–particle interaction. A cage surrounding the particle shape is used to match the flow solutions arising from a finite difference discretization with the spectral solutions of the Stokes flow. In their approach, Zhang and Prosperetti track in a Lagrangian manner the particles which are subjected to hydrodynamic and external forces. The interaction between the particles is not explicitly modeled. They have applied their numerical method to simulate the interaction between a Homogeneous Isotropic Turbulence (HIT) and particles in a periodic cubic box [25]. They have studied the effect of a two-way coupling procedure on the decaying of the turbulent kinetic energy and the mean particle displacement. Their works were restricted to low Taylor-microscale Reynolds number around 29 as their flow simulation grid was 256^3. The largest particle simulations dealing with turbulent flow at a resolved particle scale have been proposed by Uhlmann concerning the sedimentation of 1000 particles in a periodic box on a $512^2 \times 1024$ grid [26] and the turbulent interactions inside a vertical particulate channel flow [27] on a $2048 \times 513 \times 1024$ grid. The numerical methods developed in these works are based on the addition of a direct forcing in the momentum equations to account of the particle presence. The particles are tracked in a Lagrangian manner and the forcing term is also estimated with a Lagrangian approach at the center of the particles. It is redistributed as an Eulerian force thanks to kernel or discrete Dirac functions, according to Peskin work [36]. The particle interaction is treated by means of the repulsive force introduced by Glowinski [24]. A modified version of the IB method of Uhlmann has been proposed by Lucci et al. [30,31] to perform finite sized particle simulations. On a numerical point of view, their modifications concerned the time integration of the Navier–Stokes equations and the management of the two-way coupling force applied on the particles. Lucci and co-workers have investigated the modulation of a HIT flow by particles laying in the range 16 to 35 times the Kolmogorov scale at various Stokes numbers for Taylor-microscale Reynolds numbers of 75 and 110 respectively on 256^3 and 512^3 grids. Parametric studies on the density ratios between particles and fluid with a volume fraction in the range 0.01 to 0.1 have demonstrated for example that the turbulent kinetic energy was reduced by the particles compared to a reference single phase HIT flow. A different finite-size particle modeling has been proposed by Ten Cate et al. [28] which is related to lattice Boltzmann approaches. In their approach, the interaction between particles and fluid and the so the no-slip solid boundary condition is enforced through a body force added to the momentum equations. This force accounts for lubrication and repulsive effects during particle interactions. With the lattice Boltzmann model, Ten Cate and co-workers have studied the energy spectra and particle distribution functions for particles placed in a forced homogeneous turbulence for various Stokes numbers at a Taylor microscale $Re = 61$ on a 256^3 grid. Other authors have used a classical bounce-back technique for simulating the sedimentation of turbulent particle-laden flows [29]. To finish with, a wide literature has been devoted to the numerical modeling of finite size particle flows by means of fictitious domains and penalty methods [18,32,33,37]. The penalty techniques consist in playing on the magnitude of the dynamic viscosity to impose the local solid character of the medium. In recent works, an Implicit Tensorial Penalty Method (ITPM), based on a decomposition of the viscous stress tensor, has been proposed to deal with particulate flows with an accuracy between 1 and 2 in space convergence [38–40]. The ITPM has been applied to the DNS of fluidized beds containing 2133 particles by Corre et al. [10].

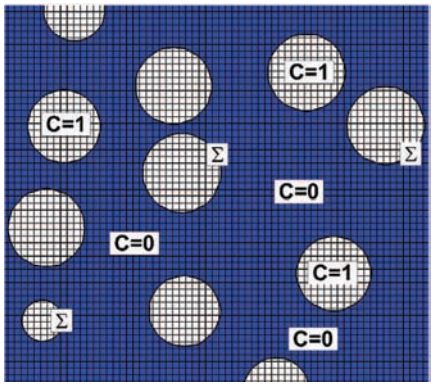


Fig. 1. Definition sketch of the fictitious domain approach for a finite size particulate flow. The underlaying grid, the phase function C and the fluid–particle interface Σ are plotted.

The present work proposes a second order in space penalty method for the DNS of particulate flows based on the ITPM. The objective is to build an as implicit as possible approach in which the particle positions are not modified after tracking with the single fluid velocity obtained on structured Cartesian mesh, even in the case where particle collisions are present. The penalty method is chosen, instead of the DLM or direct forcing approaches, for its fully coupled character, robustness and easy implementation, as it is based on the existing physical terms in the momentum conservation equations. In addition, Lagrangian VOF approaches are implemented and the single fluid formulation of Kataoka [41] is extended to the framework of fluid–solid particle interactions. The whole algorithms are parallelized with MPI instructions for dealing with large grid simulations.

The article is organized as follows. In the first part, the models and numerical methods are detailed paying attention to describing the original part of the numerical algorithms. In particular, a mixed Lagrangian–Eulerian VOF technique is used to follow the particle during time and an implicit treatment of the particle to particle or particle to wall interaction is implemented. An augmented Lagrangian approach and viscous penalty techniques are also proposed for dealing with the velocity-pressure coupling and the solid body motion. All these features are extended to parallel computations. The third section is devoted to numerical convergence exercises and physical validations. An application to a fluidized bed in a cylindrical tank is presented in the forth section. Conclusions and perspectives are finally drawn in the last section.

2. A tensorial penalty approach for finite size particulate flows

2.1. Fictitious domain framework

The numerical simulation of a particulate flow interacting with a surrounding fluid can be investigated following two different numerical strategies: unstructured or structured grids. This important choice is motivated by the representation of the complex shape involved by the interface between a fluid and thousand of moving particles. On the one hand, the more natural solution seems to be the implementation of an unstructured body-fitted grid to simulate the fluid area in the two-phase particle flow [14,21–23]. Building such a finite-volume or finite-element mesh in three-dimensions is not easy and requires automatic mesh generators as the solid particles move according to time and space. The remeshing process at each calculation step is time consuming and can be very difficult to manage automatically in computer softwares when global shape of the fluid–solid interface is complex [42]. On the other hand, it can be imagined to develop a fixed structured grid to simulate particle flows. In this case, the mesh is not adapted to the fluid–solid interfaces and includes both phases. The difficulty lies in the taking into account of the presence of particles in the fluid whose interface is not explicitly tracked by the non-conforming mesh. This type of modeling and numerical problem belongs to the class of fictitious domains [24, 43]. The modeling strategy developed hereafter is based on this approach.

Instead of solving two sets of equations, *i.e.* the classical Navier–Stokes equations in the fluid phase and the Newton–Euler equations in the solid phase, and connecting the solutions at the fluid–solid interface thanks to jump equations, as proposed for example by Delhaye [44] for fluid interfaces or by Maury [21] for particle flows, the fictitious domain method consists in introducing a phase function C to locate each medium and to formulate a global model valid in the fluid and solid parts of the flow. According to the local value of C, the physical characteristics and the conservation equations are adapted to fulfill the correct physical behavior. By definition, $C = 1$ in the solid, $C = 0$ in the fluid and the interface Σ between the fluid and solid phases is associated to the isosurface $C = 0.5$. A two-dimensional definition sketch is illustrated in Fig. 1 for the DNS of finite size particle flows.

2.2. Generalized one-fluid model for particulate flows

Incompressible two-phase flows involving a carrier fluid and a solid phase can be modeled by solving the incompressible Navier–Stokes equations together with a phase function C describing the particle phase shape evolutions through an advection equation on the corresponding phase function. As explained by Kataoka [41,45], the resulting model takes implicitly into account the jump relations at the interface [44,46] and the fluid–solid interface evolutions are taken into accounts in an Eulerian manner by the advection equation on C:

$$\nabla \cdot \mathbf{u} = 0 \tag{1}$$

$$\rho\left(\frac{\partial \mathbf{u}}{\partial t} + (\mathbf{u}\cdot\nabla)\mathbf{u}\right) = -\nabla p + \rho\mathbf{g} + \nabla\cdot\left(\mu\left(\nabla\mathbf{u} + \nabla^t\mathbf{u}\right)\right) + \mathbf{F}_{si} \tag{2}$$

$$\frac{\partial C}{\partial t} + \mathbf{u}\cdot\nabla C = 0 \tag{3}$$

where $\mathbf{u}$ is the velocity, p the pressure, t the time, $\mathbf{g}$ the gravity vector, ρ and μ respectively the density and the viscosity of the equivalent fluid. Concerning the turbulence modeling, it is assumed that all the space and time scales of the flow are solved and so that direct numerical simulations are performed with the present particulate one-fluid model. Deterministic Large Eddy Simulation (LES) models could also be used to take into account the under-resolved sub-grid scale turbulence structures [47]. However in this case, a specific attention should be paid in the vicinity of the particle–fluid interface, as specific sub-grid stress tensors arise in these zones [48]. The two-way coupling between particle and fluid motions is ensured in the momentum equations by the presence of a solid interaction force $\mathbf{F}_{si}$ which will be detailed and discussed in the following Section 2.5. This interaction force will be activated as soon as a collision between two particles or a particle and a wall will occur.

The one-fluid model is almost identical to the classical incompressible Navier–Stokes equations, except that the local properties of the equivalent fluid (ρ and μ) depends on C, the interface localization requires the solving of an additional equation on C. A specific volume force is added at the interface to account for particle collision effects. Satisfying the solid constraint in the particles requires to develop a specific model. A penalty approach on the viscosity is proposed and detailed in the next section.

2.3. Penalty methods for solid behavior and incompressibility

2.3.1. Second order implicit tensorial penalty method

As explained in the previous sections, the one-fluid model and the fictitious domain approach formulated for dealing with particle flows require to consider each different phase (fluid, solid) as a fluid domain with specific rheological property. Each sub-domain is located by a phase function C. Ensuring the solid behavior in the solid zones where $C = 1$ requires to define a specific rheological law for the rigid fluid without penalizing the velocity, as the particle velocities are not known *a priori* in the problems considered here (particle sedimentation, fluidized beds, turbulence particle interaction).

A specific model is designed for handling the solid particle behavior in the one-fluid Navier–Stokes equations. It is based on a decomposition of the stress tensor σ, which reads for a Newtonian fluid (see [49] and [50]):

$$\sigma_{ij} = -p\delta_{ij} + \lambda\nabla\cdot\mathbf{u}\delta_{ij} + 2\mu\mathbf{D}_{ij} \tag{4}$$

where λ et μ are respectively the compression and shearing viscosities and $\mathbf{D}$ is the tensor of deformation rate.

Following the work of Caltagirone and Vincent [51], the stress tensor can be reformulated so as to distinguish several natural contributions of the stress tensor dealing with compression, tearing, shearing and rotation. The interest of this decomposition is then to allow a distinct penalization of each term in order to strongly impose the associated stress. If we assume that the Navier–Stokes equations for a Newtonian fluid contain all physical contributions traducing compressibility effects, shearing or rotation, their splitting allows to act differentially on these effects by modifying the orders of magnitude of each term, through the related viscosity coefficients, directly in the motion equations.

Decomposing σ_{ij} according to the partial derivative of the velocity in Cartesian coordinates, we obtain [51]

$$\begin{aligned}\sigma = &\begin{bmatrix} -p+\lambda\nabla\cdot\mathbf{u} & 0 & 0 \\ 0 & -p+\lambda\nabla\cdot\mathbf{u} & 0 \\ 0 & 0 & -p+\lambda\nabla\cdot\mathbf{u}\end{bmatrix} + \kappa\begin{bmatrix} \frac{\partial u}{\partial x} & 0 & 0 \\ 0 & \frac{\partial v}{\partial y} & 0 \\ 0 & 0 & \frac{\partial w}{\partial z}\end{bmatrix} \\ &+ \zeta\begin{bmatrix} 0 & \frac{\partial u}{\partial y} & \frac{\partial u}{\partial z} \\ \frac{\partial v}{\partial x} & 0 & \frac{\partial v}{\partial z} \\ \frac{\partial w}{\partial x} & \frac{\partial w}{\partial y} & 0\end{bmatrix} - \eta\begin{bmatrix} 0 & \frac{\partial u}{\partial y}-\frac{\partial v}{\partial x} & \frac{\partial u}{\partial z}-\frac{\partial w}{\partial x} \\ \frac{\partial v}{\partial x}-\frac{\partial u}{\partial y} & 0 & \frac{\partial v}{\partial z}-\frac{\partial w}{\partial y} \\ \frac{\partial w}{\partial x}-\frac{\partial u}{\partial z} & \frac{\partial w}{\partial y}-\frac{\partial v}{\partial z} & 0\end{bmatrix}\end{aligned} \tag{5}$$

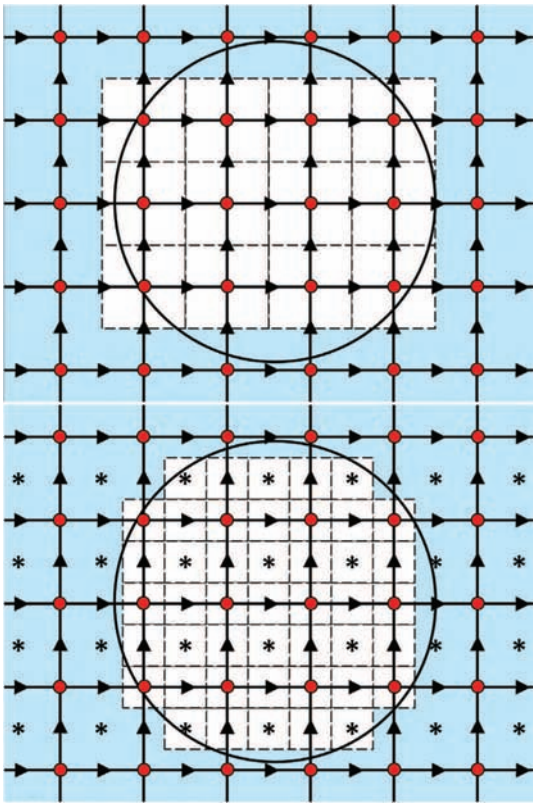


Fig. 2. Discrete interpretation of the direct viscous penalty method (top) and split viscous penalty approach (bottom) on staggered grids – the pressure points are plotted in red circles, the velocities as arrows and the pure shearing and rotations viscosities as stars. The black line represents the interface between a particle and the carrier fluid.

This decomposition of the stress tensor in which new viscosity coefficients appear artificially is written in compact form as

$$\sigma_{ij} = (-p + \lambda \nabla \cdot \mathbf{u})\delta_{ij} + \kappa \Lambda_{ij} + \zeta \Theta_{ij} - \eta \Gamma_{ij} \tag{6}$$

where λ is the compression viscosity, κ is the tearing viscosity, ζ is the shearing viscosity and η is the rotation viscosity.

The usual form of σ is easily recovered by stating $\lambda = -2/3\mu$, $\kappa = 2\mu$, $\zeta = 2\mu$ and $\eta = \mu$. As only incompressible particle flow configurations will be considered here, λ will be taken equal to zero. Finally, the divergence of the viscous stress tensor for a Newtonian fluid appearing in the one-fluid model (2) reads

$$\nabla \cdot \left(\mu\left(\nabla \mathbf{u} + \nabla^t \mathbf{u}\right)\right) = \nabla \cdot \left[\kappa \boldsymbol{\Lambda}(\mathbf{u})\right] + \nabla \cdot \left[\zeta \boldsymbol{\Theta}(\mathbf{u})\right] - \nabla \cdot \left[\eta \boldsymbol{\Gamma}(\mathbf{u})\right] \tag{7}$$

The main interest of the formulation (7) is to dissociate stresses operating in a viscous flow and then to make the implementation of a numerical penalty method easier. The use of the viscosities κ, ζ and η allows to impose a solid behavior in the zones where $C = 1$ by stating for example $\eta \gg 1$, $\kappa = 2\eta$ and $\zeta = 2\eta$ in these zones. In this case, it is imposed that the local solid flow admits no shearing, no tearing and a constant rotation according to the surrounding flow constraints. These flow constraints are implicitly transmitted to the particle sub-domain as they are solved with the fluid motion at the same time. The previous viscous penalty method is formally equivalent to choosing $\mu \gg 1$ to impose a solid behavior. However, on a discrete point of view, the two formulations are not equivalent. Indeed, on a staggered grid, the elongation viscosity is located on the pressure nodes whereas the pure shearing and rotation viscosities lie on a specific grid, at the center of the mesh grid cells, as illustrated in Fig. 2. If the dynamic viscosity μ is used to impose the solid behavior in the zones where $C = 1$, a first order convergence in space is obtained as the entire grid cell is assumed solid in this case. A rasterization effect is in this way produced at the particle–fluid interface Σ by the Direct Viscous Penalty technique (DVP). When the viscous stress tensor splitting (7) is used to impose the solid behavior, the belonging of each viscosity point to the particle can be considered (elongation viscosity on the pressure points and pure shearing and rotation viscosities on the viscous points). A more accurate accounting of the fluid–solid interface is so involved in this case thanks to the introduction of a dual grid for the pure shearing and rotation viscosities. The rasterization effect is so reduced. A second order convergence in space is obtained with the Split Viscous Penalty (SVP) formulation. These viscous penalty approaches will be discussed and compared in the validation section.

2.3.2. Augmented Lagrangian methods for multi-phase flows

Following a similar walkthrough as in the work on Stokes and Navier–Stokes equations proposed by Fortin and Glowinski [52], the augmented Lagrangian method can be applied to the unsteady Navier–Stokes equations dedicated to particulate flows. The main objective is to deal with the coupling between the velocity and pressure and to account of fluid and solid constraints. Starting with $\mathbf{u}^{*,0} = \mathbf{u}^n$ and $p^{*,0} = p^n$, the standard augmented Lagrangian solution reads

$$\begin{aligned}
&\text{while } \left\| \nabla \cdot \mathbf{u}^{*,\mathbf{m}} \right\| > \epsilon, \text{ solve} \\
&\left(\mathbf{u}^{*,0}, p^{*,0}\right) = \left(\mathbf{u}^n, p^n\right) \\
&\rho\left(\frac{\mathbf{u}^{*,m} - \mathbf{u}^{*,0}}{\Delta t} + \mathbf{u}^{*,m-1} \cdot \nabla \mathbf{u}^{*,m}\right) - \nabla\left(r \nabla \cdot \mathbf{u}^{*,m}\right) = -\nabla p^{*,m-1} + \rho \mathbf{g} + \nabla \cdot \left[\mu\left(\nabla \mathbf{u}^{*,m} + \nabla^T \mathbf{u}^{*,m}\right)\right] + \mathbf{F}_{si} \\
&p^{*,m} = p^{*,m-1} - r \nabla \cdot \mathbf{u}^{*,m}
\end{aligned} \tag{8}$$

where r is the augmented Lagrangian parameter used to impose the incompressibility constraint, m is an iterative convergence index and ϵ a numerical threshold controlling the constraint. Usually, a constant value of r is used, for example equal to the average between the minimum and maximum eigenvalues of the linear system for Stokes flows [52]. From numerical experiments, optimal values are found to be of the order of ρ_i and μ_i in each phase (fluid or solid) to accurately solve the motion equations in the related zone [38,39]. The momentum, as well as the continuity equations, are accurately described by the solution $(\mathbf{u}^*, p^*)$ coming from (8) in the medium to which the value of r is adapted. However, high values of r in the other zones act as penalty terms inducing the numerical solution to satisfy the divergence-free property only. Indeed, if we consider for example $\rho_1/\rho_0 = 1000$ (characteristic of a solid particle in air) and a constant $r = \rho_1$ to impose the divergence-free property in the particles, the asymptotic equation system solved is:

$$\begin{aligned}
&\rho\left(\frac{\mathbf{u}^* - \mathbf{u}^n}{\Delta t} + \left(\mathbf{u}^n \cdot \nabla\right)\mathbf{u}^*\right) - \nabla\left(r \nabla \cdot \mathbf{u}^*\right) = \rho \mathbf{g} - \nabla p^n + \nabla \cdot \left[\mu\left(\nabla \mathbf{u}^* + \nabla^T \mathbf{u}^*\right)\right] + \mathbf{F}_{si} \quad \text{in } \Omega_1 \\
&\frac{\mathbf{u}^* - \mathbf{u}^n}{\Delta t} - \nabla\left(r \nabla \cdot \mathbf{u}^*\right) = 0 \quad \text{in } \Omega_0
\end{aligned} \tag{9}$$

where Ω_0 and Ω_1 refer respectively to the fluid and solid phases. The idea of locally estimating the augmented Lagrangian parameter in order to obtain satisfactory equivalent models and solutions in all the media was first developed in [38] and [39]. Instead of choosing an empirical constant value of r fixed at the beginning of the simulations, and to avoid the main remaining drawback of the adaptive methods published in [38] and [39] which are linked to the *a priori* definition of dimensionless parameters for defining $r(t, M)$, it has been proposed in [53] to define the augmented Lagrangian parameter as an algebraic parameter which increases the magnitude of specific coefficients in the linear system in order to verify the divergence free constraint, while solving at same time the conservation equations. The main interests of the algebraic adaptive augmented Lagrangian method are the following: it does not require any *a priori* physical information, it applies to any kind of geometry and grid and it takes into account the residual of the linear solver and the fulfillment of incompressible and solid constraints. This version of the algebraic adapted augmented Lagrangian (3AL) method will be used in the present work, coupled to viscous penalty methods and particle interaction models. The main interest of the 3AL is that its formulation, as proposed in [53], is directly adapted to the penalization of the viscous stress tensor through the dynamic viscosity penalty or the split viscous penalty as it lies on a scanning of the matrix resulting from the discretization of the penalized conservation equations. The algorithm (8) remains valid for particulate flows with r a function of time and space of the form [53]

$$r(t)_i = \mathcal{K} \max(A_{ij},\, j = 1..N) \tag{10}$$

where i is the index of the discrete velocity solution on a grid containing N velocity points and j the index for the discretization stencil of the equation for a given ith velocity unknown. The discretization matrix containing the viscous penalty contributions is referred to as A, A_{ij} being the coefficient of A at the line i and the column j. The constant $\mathcal{K}$ is used to strengthen the penalization of the divergence free constraint in the momentum equations. It is generally chosen between 100 and 1000.

2.3.3. Physical characteristics of the equivalent fluid

The fictitious domain approach used in the present work considers the solid part of the particulate flow as a fluid with specific rheological properties whose evolutions are modeled by the Navier–Stokes equations. The present section explains how the characteristics of the solid equivalent fluid are defined to ensure a deformation free behavior in the related zones.

Classically, for any point $\mathbf{P}$ belonging to the solid zones of the calculation domain Ω, *i.e.* the zones where $C = 1$, the solid behavior is characterized by a translation and a rotation. For any particle, constant translation and rotation velocities $\mathbf{u}_0$ and $\mathbf{w}$ exist such that

$$\forall \mathbf{P} \in \boldsymbol{\Omega}^I,\ \exists \{\mathbf{w}, \mathbf{u}_0\}, \quad \mathbf{u}(\mathbf{P}) = \mathbf{u}_0 + \mathbf{X}_{\mathbf{B}}^{\mathbf{I}} \mathbf{P} \wedge \mathbf{w} \tag{11}$$

where $\mathbf{X}_\mathbf{B}^\mathbf{I}$ is the barycenter of the considered particle I and $\boldsymbol{\Omega}^I$ the related solid sub-domain. The solid constraint is intrinsically maintained if the deformation tensor is nullified:

$$\forall \mathbf{P} \in \boldsymbol{\Omega}^I, \quad \nabla \mathbf{u} + \nabla^T \mathbf{u} = 0 \tag{12}$$

In other words, if we assume that (12) is satisfied, the following systems are obtained:

$$\begin{cases} \dfrac{\partial u}{\partial x} = 0 \\ \dfrac{\partial v}{\partial y} = 0 \\ \dfrac{\partial w}{\partial z} = 0 \end{cases} \tag{13}$$

$$\begin{cases} \dfrac{\partial u}{\partial y} = -\dfrac{\partial v}{\partial x} \\ \dfrac{\partial v}{\partial z} = -\dfrac{\partial w}{\partial y} \\ \dfrac{\partial w}{\partial x} = -\dfrac{\partial u}{\partial z} \end{cases} \tag{14}$$

Then, Eqs. (13) give the direction dependencies of each velocity components as

$$\mathbf{u} = \mathbf{u}(y, z), \qquad \mathbf{v} = \mathbf{v}(x, z), \qquad \mathbf{w} = \mathbf{w}(x, y) \tag{15}$$

By using Eqs. (14), three functions $\omega_1(x)$, $\omega_2(y)$ and $\omega_3(z)$ can be defined such that

$$\begin{cases} \dfrac{\partial u(y,z)}{\partial y} = -\dfrac{\partial v(x,z)}{\partial x} = \omega_3(z) \\ \dfrac{\partial v(x,z)}{\partial z} = -\dfrac{\partial w(x,y)}{\partial y} = \omega_1(x) \\ \dfrac{\partial w(x,y)}{\partial x} = -\dfrac{\partial u(y,z)}{\partial z} = \omega_2(y) \end{cases} \tag{16}$$

If it is assumed that the rotation velocity components have the necessary regularity, the Schwarz theorem gives a constant second order derivative of the velocities:

$$\begin{cases} \dfrac{\partial^2 u(y,z)}{\partial y \partial z} = \dfrac{\partial \omega_3(z)}{\partial z} = -\dfrac{\partial \omega_2(y)}{\partial y} = W_1 \\ \dfrac{\partial^2 v(x,z)}{\partial x \partial z} = \dfrac{\partial \omega_1(x)}{\partial x} = -\dfrac{\partial \omega_3(z)}{\partial y} = W_2 \\ \dfrac{\partial^2 w(x,y)}{\partial x \partial y} = \dfrac{\partial \omega_2(y)}{\partial y} = -\dfrac{\partial \omega_1(x)}{\partial x} = W_3 \end{cases} \tag{17}$$

It can be verified that the second order derivatives are equal to zero by solving the following system:

$$\begin{cases} W_2 = -W_3 \\ W_3 = -W_1 \\ W_1 = -W_2 \end{cases} \tag{18}$$

As a consequence, the functions ω_1, ω_2 and ω_3 are constant and therefore continuous and derivable with continuous derivatives. Finally, by integrating Eqs. (17), we obtain

$$\begin{cases} u = u_0 + \omega_3 y - \omega_2 z \\ v = v_0 + \omega_1 y - \omega_3 z \\ w = w_0 + \omega_2 y - \omega_1 z \end{cases} \tag{19}$$

Eq. (11) is so verified if (12) is true. In this way, relations (11) and (12) are equivalent. Then, a solid constraint can be solved by computing $\nabla \mathbf{u} + \nabla^T \mathbf{u} = 0$. For the resolution of the momentum conservation equation (2) in the Navier–Stokes equations, this condition is asymptotically verified when $\mu \to +\infty$, as explained in Section 2.3.1.

According to the decomposition of the viscous stress tensor introduced in Section 2.3.1, an equivalent condition to (11) or (12) is to satisfy

$$\Lambda(\mathbf{u}) = 0 \tag{20}$$

$$\Gamma(\mathbf{u}) = 2\Theta(\mathbf{u}) \tag{21}$$

Indeed, it can be verified that $\nabla\mathbf{u} + \nabla^T\mathbf{u} = 2\Lambda(\mathbf{u}) + 2\Gamma(\mathbf{u}) - \Theta(\mathbf{u})$. For any Newtonian fluid or solid media, the relations $\kappa = 2\mu$, $\zeta = 2\mu$ and $\eta = \mu$ must be satisfied, as proposed in Section 2.3.1, together with $\mu \gg 1$ in the particles.

Numerically, Eqs. (12), (20) and (21) have to be implemented on the split viscous penalty grid described in Section 2.3.1 in Fig. 2. For internal solid nodes (those where $C = 1$) the solid viscosity is chosen to be 100 to 1000 times the viscosity of the carrier fluid. This choice will be discussed in the validation section concerning the accuracy of the simulations and the effect on the cost of the linear solvers. The previous remarks on the order of magnitude of the viscosity inside the solid parts stand for the continuous point of view.

On a discrete point of view, the flow grid cells cut by the fluid–solid interface Σ must be distinguished compared to those entirely included in the particles. For these last nodes, the dynamic viscosity is chosen equal to $\mu_\infty \approx K\mu_{\text{carrier fluid}}$ with $100 \leqslant K \leqslant 1000$. For the fluid–solid cells, different methods can be used to define the homogenized viscosity. First, to avoid any direct interpolation of the viscosity coefficients associated to off diagonal viscous stress tensor components, an interpolation C_μ of the volume fraction is defined at the viscosity nodes, *i.e.* stars in Fig. 2 on the split viscous penalty grid:

$$C_\mu = \frac{1}{4}\sum_N C_N \tag{22}$$

where N denotes the indices of the pressure nodes located at the vertices of the cell to which C_μ belongs. Four different numerical viscous laws have been investigated according to C for the diagonal viscous stress tensor terms, *i.e.* red circles in Fig. 2, C_μ and also a conditional indicator function I_C satisfying $I_{C<0.5} = 1$ if $C < 0.5$ or $I_{C\geqslant 0.5} = 1$ if $C \geqslant 0.5$:

1. Numerical viscous law 1 (NVL1), the viscosity is defined in a discontinuous way according to C_μ:
   $\kappa = 2[\mu_f I_{C<0.5} + \mu_s I_{C\geqslant 0.5}]$
   $\zeta = 2[\mu_f I_{C_\mu<0.5} + \mu_s I_{C_\mu\geqslant 0.5}]$
   $\eta = \mu_f I_{C_\mu<0.5} + \mu_s I_{C_\mu\geqslant 0.5}$
2. Numerical viscous law 2 (NVL2), the viscosity is given by an arithmetic average:
   $\kappa = 2[(1-C)\mu_f + C\mu_s]$
   $\zeta = 2[(1-C_\mu)\mu_f + C_\mu\mu_s]$
   $\eta = (1-C_\mu)\mu_f + C_\mu\mu_s$
3. Numerical viscous law 3 (NVL3), the viscosity is given by a harmonic average:
   $\kappa = 2[\frac{\mu_f\mu_s}{C\mu_f+(1-C)\mu_s}]$
   $\zeta = 2[\frac{\mu_f\mu_s}{C_\mu\mu_f+(1-C_\mu)\mu_s}]$
   $\eta = \frac{\mu_f\mu_s}{C_\mu\mu_f+(1-C_\mu)\mu_s}$
4. Numerical viscous law 4 (NVL4), the viscosity is defined with a mixed average as proposed by Benkenida and Magnaudet [54]:
   $\kappa = 2[(1-C)\mu_f + C\mu_s]$
   $\zeta = 2[\frac{\mu_f\mu_s}{C_\mu\mu_f+(1-C_\mu)\mu_s}]$
   $\eta = \frac{\mu_f\mu_s}{C_\mu\mu_f+(1-C_\mu)\mu_s}$

Concerning the density, an arithmetic average is used whatever its location on the discretization grid. The most clever choice of viscosity average for the ITPM will be discussed in the validation section.

2.4. Eulerian–Lagrangian VOF method for particle tracking

Once the particle center of mass is known in the computations, it has been explained that the ITPM requires to locate the interior and exterior of the particle thanks to a phase function C in order to build the physical properties of the equivalent fluid such as the dynamic viscosity. This section explains how at each time step the finite size particles are advected and how the solid fraction C is obtained on the Eulerian flow grid.

At each time step, the mass and momentum equations are solved by using the augmented Lagrangian approach explained before including the particle–particle collision forces $\mathbf{F}_{si}$ detailed in Section 2.5. Thanks to the ITPM, the one-fluid velocity field provides the solid velocity field inside the particles. Then, instead of using a classical Eulerian VOF approach [53,55,56] to obtain the new solid fractions in each Eulerian cells by solving Eq. (3), the Lagrangian velocities $\mathbf{V}^{I,L}$ of each particle, located in a Lagrangian way by their position $\mathbf{X}^{I,L}$, are computed at reference points (the four green points in Fig. 3, in the two-dimensional configuration) located inside each particle by using an interpolation method explained in Section 2.4.1. The new positions of the particles are then updated in a Lagrangian manner, as developed in Section 2.4.2 and finally the new Eulerian solid fractions are estimated by means of a projection of the exact shape of the particles on the flow grid. This last step is detailed in Section 2.4.3. The interest of using a Lagrangian scheme to advect the particles and to project their shape

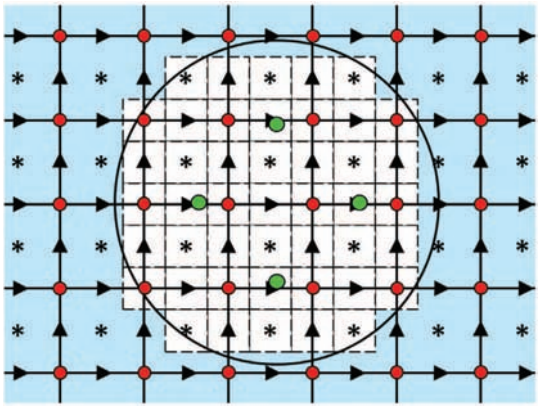


Fig. 3. Position in two dimensions of the reference Lagrangian points (green points) used to interpolate the Lagrangian velocity at the barycenter of the particles. (For interpretation of the references to color in this figure, the reader is referred to the web version of this article.)

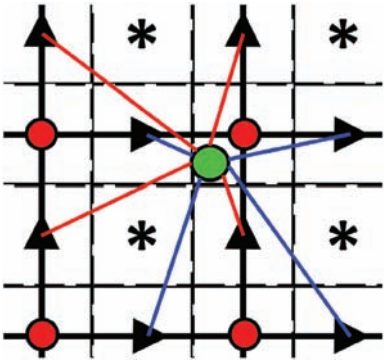


Fig. 4. Eulerian velocity kernel (u-components in blue and v-components in red) used in two dimensions to estimate the components of the interpolation Lagrangian velocity points (green point). (For interpretation of the references to color in this figure, the reader is referred to the web version of this article.)

on the Eulerian mesh is to avoid any distortion of the particle shape over time, as would be induced by a classical Eulerian VOF scheme.

2.4.1. Computation of particle velocity

The Lagrangian particle velocity located at the center of each solid sphere is computed by using 4 or 6 points respectively in two or three dimensions. The same procedure allows to estimate the rotation velocity if required. In Fig. 3, the position of the velocity calculation point, colored in green, is represented for the two-dimensional case. These points are positioned on the axis parallel to the Cartesian coordinate system axis, at half the radius of the particles on each side of the center of the spheres. We have observed that it was more accurate to define the Lagrangian velocity of the particles by using fixed points located inside the frame of the particles compared to an Eulerian average of the velocity field inside each solid sphere. A lower accuracy has been also obtained with the use of a kernel based interpolation [57]. With the proposed four or six point approach, the idea is to estimate the Lagrangian velocity $\mathbf{V}^{I,L}$ at the barycenter of the spheres by interpolating it at the $\mathbf{X}_k^{I,L}$ locations according to the surrounding Eulerian solid velocity field. Index I stands for the number of the particle and $k = 1..N$ for the number of the interpolation point associated to particle I, with $N = 4$ in 2D and $N = 6$ in 3D. The velocity is interpolated from the nearest Eulerian velocity node values as shown in Fig. 4 for the two-dimensional case. The relative positions $\tilde{X}$ of the interpolation points compared to the Eulerian velocity components $X_{\mathbf{u}}$ and particle center $\mathbf{X}^{I,L}$ is first calculated as

$$\tilde{\mathbf{X}} = \begin{pmatrix} \tilde{x} \\ \tilde{y} \\ \tilde{z} \end{pmatrix} = \frac{\mathbf{X}_k^{I,L} - \mathbf{X}_{\mathbf{u}}}{\mathbf{DX}^{I,L}} \tag{23}$$

where for a given interpolated Lagrangian velocity component, $\mathbf{DX}^{I,L}$ refers to the distance vector in each Cartesian coordinate between two opposite points of the box (parallelepiped in three dimensions) formed by the Eulerian velocity components used for the interpolation. In two dimensions, the surrounding Eulerian components used to interpolate $\mathbf{V}_k^{I,L}$ are represented in Fig. 4 with blue (u-component) and red (v-component) lines joining the Lagrangian interpolation position $\mathbf{X}_k^{I,L}$.

The basis P_m, $m = 1..N$ of the bilinear interpolation is then built according to the n ($n = 4$ in 2D and $n = 8$ in 3D) Eulerian velocity components V_n as follows

$$P_1 = V_1 \tag{24}$$
$$P_2 = V_2 - V_1 \tag{25}$$
$$P_3 = V_4 - V_1 \tag{26}$$
$$P_4 = V_1 + V_3 - V_2 - V_4 \tag{27}$$

in two dimensions and

$$P_1 = V_1 \tag{28}$$
$$P_2 = V_2 - V_1 \tag{29}$$
$$P_3 = V_4 - V_1 \tag{30}$$
$$P_4 = V_5 - V_1 \tag{31}$$
$$P_5 = V_3 + V_1 - V_2 - V_4 \tag{32}$$
$$P_6 = V_6 + V_1 - V_2 - V_5 \tag{33}$$
$$P_7 = V_8 + V_1 - V_4 - V_5 \tag{34}$$
$$P_8 = V_7 - V_6 - V_8 + V_5 \tag{35}$$

in three dimensions. The lth component of the Lagrangian interpolated velocity is obtained by

$$V_{k,l}^{I,L} = P_1 + P_2\tilde{x} + P_3\tilde{y} + P_4\tilde{x}\tilde{y} \quad \text{in 2D} \tag{36}$$
$$V_{k,l}^{I,L} = P_1 + P_2\tilde{x} + P_3\tilde{y} + P_4\tilde{z} + P_5\tilde{x}\tilde{y} + P_6\tilde{x}\tilde{z} + P_7\tilde{z}\tilde{y} + P_8\tilde{x}\tilde{y}\tilde{z} \quad \text{in 3D} \tag{37}$$

Finally, the Lagrangian velocity at the barycenter of the particle reads

$$\mathbf{V}^{I,L} = \frac{\sum_N \mathbf{V}_k^{I,L}}{N} \tag{38}$$

2.4.2. Transport of the particles

Once the Lagrangian particle velocity is known by (38), the particles are advected in a Lagrangian manner by an update of the position of their mass center $\mathbf{X}^{I,L}$ as follows

$$\mathbf{X}^{I,L,n+1} = \mathbf{X}^{I,L,n} + \Delta t \mathbf{V}^{I,L,n+1} \tag{39}$$

with the second order Lagrangian velocity extrapolation at time $(n+1)\Delta t$ being given by

$$\mathbf{V}^{I,L,n+1} = \frac{\mathbf{V}^{I,L,n} + \mathbf{V}^{I,L,n+1/2}}{2} \tag{40}$$

The intermediate Lagrangian particle velocity is defined according to the interpolated position of the particle I at time $(n+1/2)\Delta t$, which is given by $\mathbf{X}^{I,L,n+1/2} = \mathbf{X}^{I,L,n} + \Delta t \mathbf{V}^{I,L,n}$, as follows

$$\mathbf{V}^{I,L,n+1/2} = \frac{\sum_N \mathbf{V}_k^{I,L,n+1/2}}{N} \tag{41}$$

The Lagrangian particle advection scheme (39)–(41) corresponds to a second order accurate in time Runge–Kutta scheme.

2.4.3. Update of the solid fraction

The one-fluid model used to simulate the particle flow does not explicitly use the Lagrangian positions or velocities of the solid spheres. As a fictitious domain approach, it requires the accounting of the Eulerian solid fraction C in each Eulerian grid cell. The phase function C have to be computed according to the Lagrangian position of particles at time $(n+1)\Delta t$ instead of solving explicitly the Eulerian advection equation on C. This is achieved by generating a set of virtual test points on a regular network inside each pressure control volume, as described for the two-dimensional case in Fig. 5. On a statistical point of view, the local solid fraction in a given control volume is naturally defined by the number of virtual points belonging to the interior of the particle normalized by the total number of virtual points used in the control volume.

The effect of the number of virtual points on the accuracy of the surface of the particle projected on the Eulerian flow grid is proposed in Fig. 6. Various Eulerian grids are considered, *i.e.* G_1, G_2, G_3, G_4 and G_5, containing respectively 5, 10, 20, 40 and 80 discretization points along a particle diameter. It is observed that even with only 5 Eulerian grid points for a

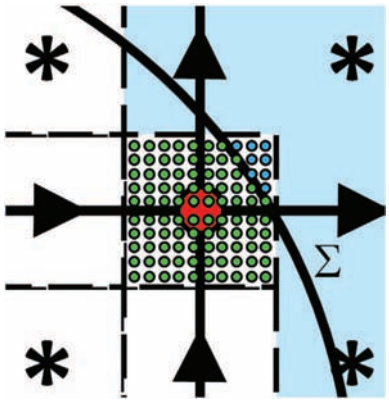


Fig. 5. Two-dimensional network of 10^{Ndim} virtual points used to estimate the local solid fraction C^{n+1} thanks to a Lagrangian position $\mathbf{X}^{l,L,n+1}$ of a particle, whose interface is noted Σ. In green are plotted the virtual points belonging to the particle and in blue the other ones. In the example, $C^{n+1} = 92/100 = 0.92$. (For interpretation of the references to color in this figure, the reader is referred to the web version of this article.)

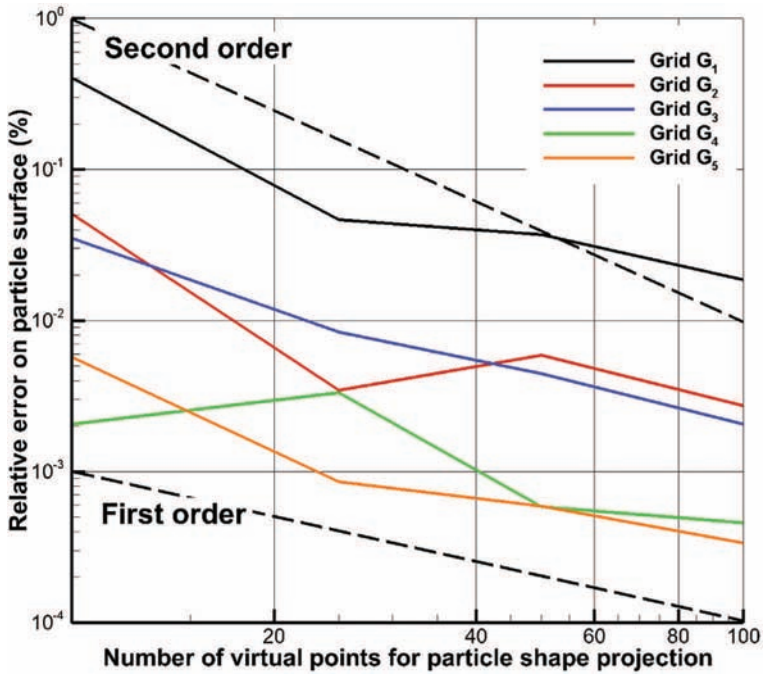


Fig. 6. Error on the projected surface of a circular shape particle according to the number of virtual points in each space direction and to the Eulerian grid used.

particle diameter, the relative error on the particle shape is less than 0.1%. Increasing the number of virtual points reduces the error on the particle surface, with a convergence order between 1 and 2. The network of virtual points which will be considered in our simulations will be composed of 25^{Ndim} points, with *Ndim* the number of dimensions of the problem. Indeed, it can be observed that in this case, the error on the solid fraction estimate is always less than 0.1% whatever the computational flow grid. This constraint is important to deal with DNS of particulate flows as only a moderate number of Eulerian cells along a particle diameter can be used in three-dimensional simulations to simulate realistic problems.

2.5. Numerical modeling of particle interaction

Leading fully resolved particulate simulations requires to manage the contact and collisions between particles in order to prevent overlapping between particles or particles and walls. This spurious numerical phenomenon is in particular induced by the approximation of the particle trajectories and the projection of the spherical shape on the Eulerian grid. For volume ratios of particles lower than 0.1%, collisions are often assumed negligible [58,59]. As soon as a general particulate flow model is built for low and high solid fractions, the collisions can be a major physical phenomenon, such as in fluidized beds.

The fully resolved numerical simulations have to integrate a collision model to prevent unphysical adhesion of particles and try to represent reality. This point is developed in the present section.

2.5.1. Existing models for particle interaction

A first approach consists in defining a mass-damping force [10,24] or an exponential repulsive force [18] that ensures that particles do not collide. These methods do not include *a priori* the explicit modeling of the influence of the lubrication effects. Several solutions exist to account for lubrication: the first one is based on a local refinement of the flow grid in order to resolve the lubrication effect [60,61]. Therefore, this approach is very expensive in three dimensions. Another solution consists in adding an equivalent force to the repulsive component in order to reproduce the lubrication force. We have chosen this strategy, based on the work of Breugem [62].

2.5.2. Solid/solid collision

A normal solid/solid collision is characterized by the dry coefficient of restitution (in air), e_d, defined as the ratio between the velocity after and before the collision. The energy absorbed by the collision is represented by the e_d coefficient. For a solid collision between steel spheres, the collision time is around 10^{-9} seconds. This time is too small to be reproduced by the fluid simulation with a time step chosen according to macroscopic hydrodynamic effects, with Δt laying in the range 10^{-6}–10^{-2} s in most of the fluid mechanics problems involving particles such as a fluidized bed or a sedimentation flow. The solution in which a repulsive force is used to prevent from particle numerical adhesion is known as smooth spheres [63]. The main drawback of this model is that it artificially separate particles or walls as soon as they are distant from one grid cell. In this way, the collision effect is not accurately modeled and the restitution coefficient is generally underestimated.

In order to account explicitly for the restitution coefficient, a damping-mass force is used, instead of a standard smooth sphere repulsive force, according to Eq. (42) where $N_c \Delta t$ represents the collision time, which is always overestimated. Preliminary tests have shown that using $N_c = 8$ is a good compromise to get a correct collision model (more details on the numerical implementation are given in [64])

$$\mathbf{F_s} = \frac{m_e(\pi^2 + \ln(e_d)^2)}{[N_c \Delta t]^2}\mathbf{d} - \frac{2m_e \ln(e_d)}{[N_c \Delta t]}\dot{\mathbf{d}} \tag{42}$$

where m_e is the reduced mass verifying $m_e = (m_1^{-1} + m_2^{-1})^{-1}$ for inter-particle collision and $m_e = m$ for particle wall collision, $\mathbf{d}$ is the distance vector in each Cartesian direction between the particles or the particle and the wall and $\dot{\mathbf{d}}$ is the time derivative of $\mathbf{d}$. Notations m_1 and m_2 stand for the masses of particle 1 and 2 whereas m denotes the mass of the particle in a particle/wall collision configuration. The restitution coefficient is given by the user depending on the material and particle properties. This input parameter have to be measured experimentally.

2.5.3. Lubrication

Many authors propose models that include the lubrication effects [60,65,66]. The principle consists in utilizing the analytical development given by [67] or the lower order development provided by [63] of the forces exerted by a viscous fluid between two particles or a particle and a wall. The following formulation of the lubrication force is considered here:

$$\mathbf{F_l}(\epsilon_i, \mathbf{u}_n) = -6\pi \mu_f R \mathbf{u}_n \left[\lambda(\epsilon_i) - \lambda(\epsilon_{al})\right] \tag{43}$$

with λ being defined for particle–particle interaction as λ_{pp} or as λ_{pw} for particle–wall interaction

$$\lambda_{pp} = \frac{1}{2\epsilon_i} - \frac{9}{20}\log(\epsilon_i) - \frac{3}{56}\epsilon_i \log(\epsilon_i) + 1.346 + \bigcirc(\epsilon_i) \tag{44}$$

$$\lambda_{pw} = \frac{1}{\epsilon_i} - \frac{1}{5}\log(\epsilon_i) - \frac{1}{21}\epsilon_i \log(\epsilon_i) + 0.9713 + \bigcirc(\epsilon_i) \tag{45}$$

where $\mathbf{u}_n$ is the normal velocity between the particles or the particle and the wall, and $\epsilon_i = \frac{\|\mathbf{d}\|}{R}$ is the dimensionless distance between them. The activation distance ϵ_{al} is given by numerical assumptions explained in [64].

2.5.4. Four-way coupling

The modeling and simulation of fully resolved particles is intrinsically based on two-way coupling approaches, in which the effect of the fluid on the particles and the modification of the carrier fluid due to the particle motions are explicitly solved. Several reference works exist on this topic [25–27,30–33,39]. In these models, it is assumed that the flow grid is refined enough to undertake the lubrication or collision effects or that the solid concentrations are sufficiently low [59,68] such that the collision frequency is low too.

As soon as the flow grid and time steps are coarse compared to the lubrication and collision characteristic time and space scales, an explicit modeling of the collision and lubrication forces have to be added to the particle flow model, as discussed for example by [69]. When relevant particle/particle interactions such as turbulent dispersion, transverse lift forces, wall collisions with roughness or inter-particle collisions, are explicitly accounted by the models, the particle model is called four-way coupling. Our finite size particle flow model belongs to this class of approaches, as previously published

by [24,34]. To our opinion, the works of [26,27,30,31] are also four-way coupling based finite size particle models, even if their authors consider them as two-way coupling, as they explicitly account for particle collision. The main originality of our particle collision modeling is the implicit treatment of the collision forces directly in the momentum equations.

Instead of taking into account the particle collisions explicitly during the particle tracking step, it has been chosen to directly plug the resulting interaction forces $\mathbf{F_s}$ and $\mathbf{F_l}$ into the momentum equations. The Lagrangian collision force for a particle I is $\mathbf{F}_{si}^{I} = \mathbf{F_s} + \mathbf{F_l}$. It is projected as a volume force in the momentum equations so as to implicitly prevent particle sticking or penetration during the global one-fluid velocity solving. The two forces $\mathbf{F_s}$ and $\mathbf{F_l}$ are estimated thanks to an extrapolated position of each particle $\mathbf{X}^{I,L,n+1}$ at time $(n+1)\Delta t$ with the use of the velocity at the preceding time step. This choice avoids a time splitting error induced by an explicit treatment of the collision, as in the works of [10,24–27, 30,31,33,34]. This point is the main difference between our implementation and the implementation of the collision force given by [62]. Then, the Lagrangian forces for each particle I are distributed in the Eulerian cells included inside the particle shape by

$$\mathbf{F}_{si}(M) = \mathbf{F}_{si}^{I}/(V_p) \tag{46}$$

if Eulerian grid point M is inside particle I. The particle volume is referred to as V_p. The implicit treatment of lubrication and solid–solid collision forces has been validated in [64] against the experiments and correlation of [70] concerning the restitution coefficient of a particle after a collision with a solid wall. By implicit treatment, it is considered that the particle overlapping is avoided directly during the solving of the pressure and velocity field by a time extrapolation of the particle collision force. In reality, this numerical treatment is semi-implicit as the particle position is not updated during the solving of the mass and momentum equations.

2.6. General numerical methods

From a general point of view, the one-fluid Navier–Stokes equations are discretized in Thétis, a CFD code developed in the I2M Institute in the TREFLE Departement, with implicit finite-volumes on an irregular staggered Cartesian grid. A second-order centered scheme is used to approximate the spatial derivatives while a second-order Euler or Gear scheme is used for the time integration. All the terms are written at time $(n+1)\Delta t$, except the inertial term which is linearized as follows:

$$\mathbf{u}^{n+1} \cdot \nabla \mathbf{u}^{n+1} \approx \left(2\mathbf{u}^{n} - \mathbf{u}^{n-1}\right) \cdot \nabla \mathbf{u}^{n+1} \tag{47}$$

It has been demonstrated that this approximation allows to reach a second-order convergence in time [71]. The coupling between velocity and pressure is ensured with an implicit algebraic adaptive augmented Lagrangian method. The augmented Lagrangian methods presented in this work are independent on the chosen discretization and could be implemented for example in a finite-element framework [72]. In two-dimensions, the standard augmented Lagrangian approach [52] can be used to deal with two-phase flows as direct solvers [73] are efficient in this case. However, as soon as three-dimensional problems are under consideration, the linear system resulting from the discretization of the augmented Lagrangian terms has to be treated with a BiCGSTAB II solver [74], preconditioned by a Modified and Incomplete LU method [75]. Indeed, in three-dimensions, the memory cost of direct solvers makes them impossible to use. The 3AL method presented before is a kind of general preconditioning which is particularly efficient when multi-phase or multi-material flows are undertaken, *i.e.* when sharp density or viscosity gradients occur. The numerical methods and the one-fluid model have been validated by the authors concerning single particle flows in [33] and [39].

2.7. Parallel implementation

Thétis simulation tool has been parallelized for distributed memory architectures with MPI procedures. The parallelism is based on a grid decomposition to which the same simulation algorithm is applied on each processor. Each processor possesses its own data with specific node covering zones used to exchange the solutions at the boundaries of the processor data blocs. On each processor data block, a standard BiCGSTAB II solver is used which is preconditioned thanks to the local available unknowns through a Modified and Incomplete LU (MILU) method. The grid splitting is simply achieved by using a Cartesian cutting in each direction of the global mesh covering all the mesh blocks associated to each processor. More details on the parallelism is given in [76].

Specific developments have been investigated concerning the tracking of the particles over time in processor discrete space. Indeed, to build the phase function describing the local solid fraction and to update at each time step the physical characteristics of the one-fluid equations, the searching of particles interacting with a solid sphere belonging to a given processor must be undertaken. This type of algorithms has been often studied for many applications as the simulation of granular flows, the molecular dynamics or the universe gravitational forces. The algorithms change depending on the range of the interactions. For short range interactions the existing methods are able to find collisions between millions of particles. The most common algorithms use linked list approach [77,78], Verlet list [79] or a combination of the two [80]. These algorithms are designed to deal with millions of particles efficiently. In our case they are not straightforwardly required because the number of considered particles is around several thousands and the number of CPU used for the

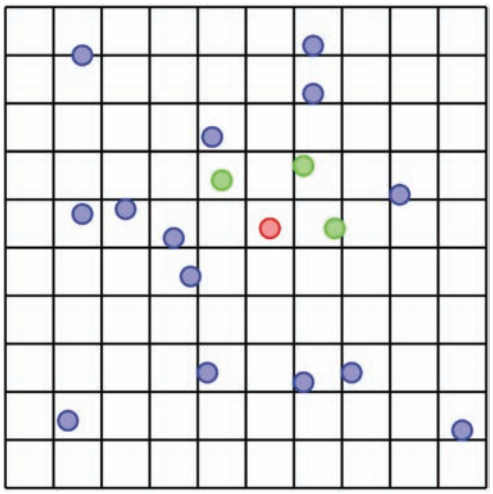


Fig. 7. Searching of particle collision inside a CPU box distribution of 10×10 in two dimensions – the red particle is detected to interact with green particles whereas no interaction is considered with the blue ones. (For interpretation of the references to color in this figure, the reader is referred to the web version of this article.)

simulations is determined by the needs of the fluid solver and the expected precision of the physical solution. However, brute force algorithm that search all the collisions between all the particles have a complexity of $\mathcal{O}(N_p^2)$ if N_p is the number of particles. The time spent in searching collisions becomes important, *i.e.* comparable or larger than the solving time of the Navier–Stokes equations, for $N_p \geqslant 500$ with such a direct approach. A finer implementation using for example octree structures will be required in the future to improve this aspect.

As a consequence, it has been decided to implement a cell-list approach to reduce the CPU time involved by the particle searching. The main idea is to split the physical space in boxes, and to search for collisions between particles only in a given box and the boxes around, as illustrated in Fig. 7. Two conditions are necessary, the particles cannot pass through a box during a time step and the length of the boxes cannot be lower than the particle radius. The first condition is satisfied by assuming a CFL condition less than 1. The second condition have to be respected by the definition of the boxes. In our case, the CPU boxes generated by the Cartesian splitting of the global mesh are optimum for the solver with a number of cells of about 30^3. As the particle considered in our simulations have between 8 and 15 grids cells per radius, this condition is always fulfilled. Therefore, the use of the CPU boxes for the searching algorithm is a simple and efficient solution. In addition, this choice minimizes the communications between CPU.

2.8. Sum up of the implemented Eulerian–Lagrangian algorithm

The global algorithm used to solve one time iteration of fluid–particle interaction with the ITPM, the augmented Lagrangian approach and the Lagrangian VOF particle tracking is summarized in Fig. 8. The first part of this work flow is devoted to predicting the position of the particle at time $(n+1)\Delta t$ through an extrapolation of their trajectories. The four-way coupling forcing terms $\mathbf{F}_{si}^n$ are deduced from the particle interaction at this tentative position. The mass and momentum equations are then solved in both fluid and solid zones to obtain the pressure and velocities at time $(n+1)\Delta t$. The particles are finally advected in a Lagrangian way with the new velocity field. At the end of each time iteration, Lagrangian positions of the particles are projected on the Eulerian grid to build C^{n+1} and the local densities and viscosities are updated according to C^{n+1} before starting the next physical time iteration. This last procedure allows to penalize the solid behavior according to penalty viscosities in the cells belonging to the particles and also to account for buoyancy effects through the density variations.

3. Numerical and physical validations in dilute particle-laden flows

On a general point of view, the development of the ITPM method started in 1997 and is associated to previous works and publications. The complete and second order version of the method with collisions which is presented here is original. Specific validation test cases are reported here to demonstrate the numerical and physical capabilities of the method. However, the reader is encouraged to refer also to previous publications [32] or [33] for complementary test cases such as the well-known Drafting–Kissing–Tumbling (DKT) problem.

3.1. Settling of a cylindrical shape particle

The settling of a cylindrical shape particle is first considered in two dimensions in order to characterize the effect of numerical parameters such as the solver, the augmented Lagrangian parameter or the magnitude of the viscous penalty

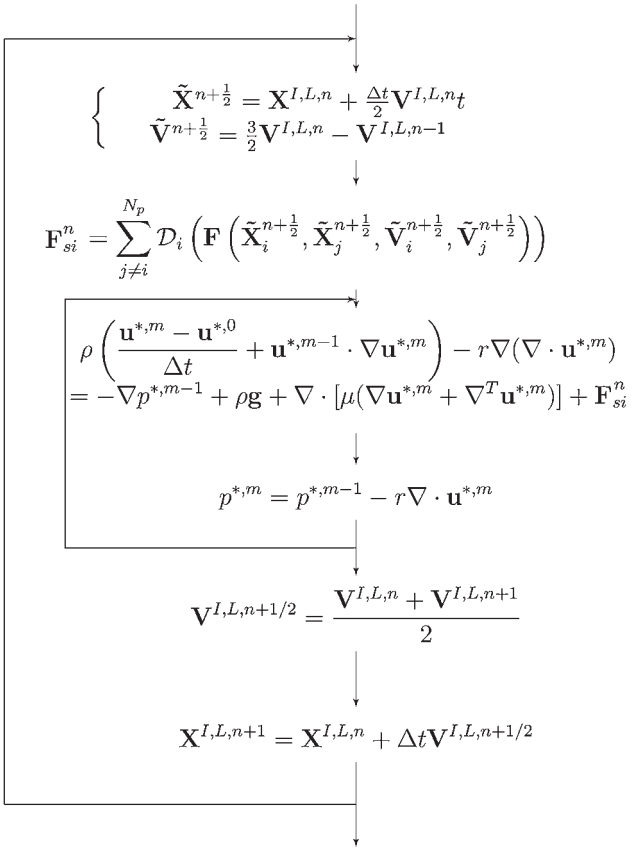


Fig. 8. Work-flow of the four-way coupling with the ITPM associated to augmented Lagrangian approach and Lagrangian VOF particle tracking.

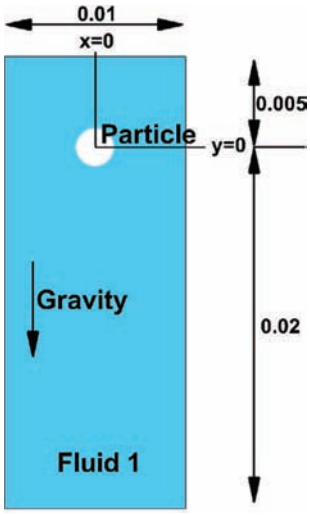


Fig. 9. Definition sketch of the settling of a cylindrical shape particle.

viscosity on the accuracy of the ITPM. The boundaries of the numerical domain are walls with a no-slip condition. A convergence study is also provided. The definition sketch of the problem is illustrated in Fig. 9. At low Reynolds number, the analytical developments of Faxen [50] can be used to estimate the resistance force F_r of the fluid on the cylindrical shape particle and its final settling velocity U_∞. This reference velocity will be used to discriminate the most efficient numerical parameters of the ITPM and also to estimate the convergence order of the method. The resistance force F_r reads

$$F_r = \frac{4\pi \mu_f U_\infty}{\ln(1/a_r) - 0.9157 + 1.7244 a_r^2 - 1.7302 a_r^4} \tag{48}$$

with a_r the aspect ratio between the particle diameter and the width of the fluid container. Index f denotes the fluid properties. The fluid resistance to the particle is compensated by buoyancy forces when the particle has reached its settling velocity U_∞. In this way,

$$F_r = (\rho_f - \rho_p)\pi R_p^2 g \tag{49}$$

where g is the magnitude of gravity, R_p the particle radius and index p refers to the particle properties. Finally, the particle settling velocity can be obtained as

$$U_\infty = \frac{(\rho_f - \rho_p) R_p^2 g [\ln(1/a_r) - 0.9157 + 1.7244 a_r^2 - 1.7302 a_r^4]}{4\mu_f} \tag{50}$$

The characteristics of the problem are the following concerning the fluid and particle properties

$$\rho_p = 200 \text{ kg m}^{-3} \tag{51}$$

$$50 \leqslant \mu_p \leqslant 50000 \text{ Pa s} \tag{52}$$

$$\rho_f = 100 \text{ kg m}^{-3} \tag{53}$$

$$\mu_f = 5 \text{ Pa s} \tag{54}$$

whereas $R_p = 0.001$ m, $a_r = 0.2$ and $g = 9.81 \text{ m s}^{-2}$. The magnitude of the analytical particle settling velocity is $U_\infty = 0.37275 \times 10^{-4} \text{ m s}^{-1}$. The corresponding particle Reynolds number is $Re_p = \frac{2\rho_p R_p U_\infty}{\mu_f} = 1.5 \times 10^{-6}$, which is in agreement with the Stokes approximation used by Faxen.

Five grids are used in the numerical simulations with a constant space step and the viscous law NVL3. They are referred to as G_1, G_2, G_3, G_4 and G_5 and are associated respectively to 50×125, 100×250, 200×500, 400×1000 and 800×2000 grid cells. Three time steps are also considered, namely $\Delta t_1 = 10$ s, $\Delta t_2 = 1$ s and $\Delta t_3 = 0.1$ s and 25 virtual particles per direction for shape projection are used.

3.1.1. Investigation of numerical parameters

The effect of the solver used to obtain the solution of the momentum conservation equations approximated by the adaptive augmented Lagrangian method is first considered with grid G_4, time step Δt_2 and penalty viscosity $\mu_p = 5000$ Pa s. The PARDISO direct solver [73] and the iterative BiCGSTAB II solver [74] are first compared, with various values of $\mathcal{K}$ used in Eq. (10). It is well known that the 3AL approach [53] is part of penalty methods and that the higher $\mathcal{K}$ is, the higher the conditionning of the discretization matrix is. The direct solver provides reference values as it is not sensitive to the conditionning of the matrix, contrary to the iterative solver. The first parametric study is investigated on the effect of the viscosity ratio across the interface and also on $\mathcal{K}$ on the efficiency of the iterative solver, as presented in Fig. 10. In this case, the number of convergence iterations at each time step is imposed to be 100, to maintain a computational time comparable to the one induced by the direct solver. It is observed that for large values of viscosity ratios and $\mathcal{K}$, the iterative solver is not able to provide a correct settling velocity in 100 iterations, as the conditionning is too important in these cases. The best solution is obtained for a viscosity ratio of 100 and a augmented Lagrangian parameter $\mathcal{K} = 100$. For small values of $\mathcal{K}$, the relative error on U_∞ is larger as the divergence free constraint is not maintained in this case. For $\mathcal{K} = 100$ and a viscosity ratio of 100, the error brought by the two solvers are comparable. These values will be used in the following sections to simulate in particular three-dimensional flows.

The second interesting and crucial parameter which is studied is the viscosity ratio at the interface. A PARDISO solver is used on the G_4 grid with Δt_2 and $\mathcal{K} = 10^8$ in this case, in order to reach an almost computer error divergence accuracy at each calculation time. The relative errors are plotted in Fig. 11. As expected, it is observed that these errors decrease linearly for increasing viscosity ratios at the interface. With the selected numerical parameters, the error is reduced from almost 0.6 to almost 0.02 percents by multiplying by 100 the viscosity ratio.

To finish with investigations of numerical behavior of ITPM, the performances of the global method (Navier–Stokes solving, particle tracking,...) are evaluated on a parallel computer. The following numerical parameters are chosen, the same as those that will be used in the validations and applications presented later in the present article: grid G_5, time step Δt_2, iterative solver, viscosity ratio of 100 and $\mathcal{K} = 10^2$. In Fig. 12 are presented the results obtained for simulations driven on 8 to 64 processors during one hour of CPU time. The theoretical speed-up curve is provided in long dashed line, corresponding to a multiplication of the reference number of time iterations on 8 processors by the number of used processors divided by 8. It is observed that the numerically obtained speed-up is 1 until 32 processors, and remains equal to 0.94 for 64. This last value corresponds to parallel blocs of 25 000 Eulerian grid cells in this case, which appears to be the limit of bloc size to maintain a good parallel acceleration of computational time. Hence, the ITPM is nicely implemented on parallel architectures.

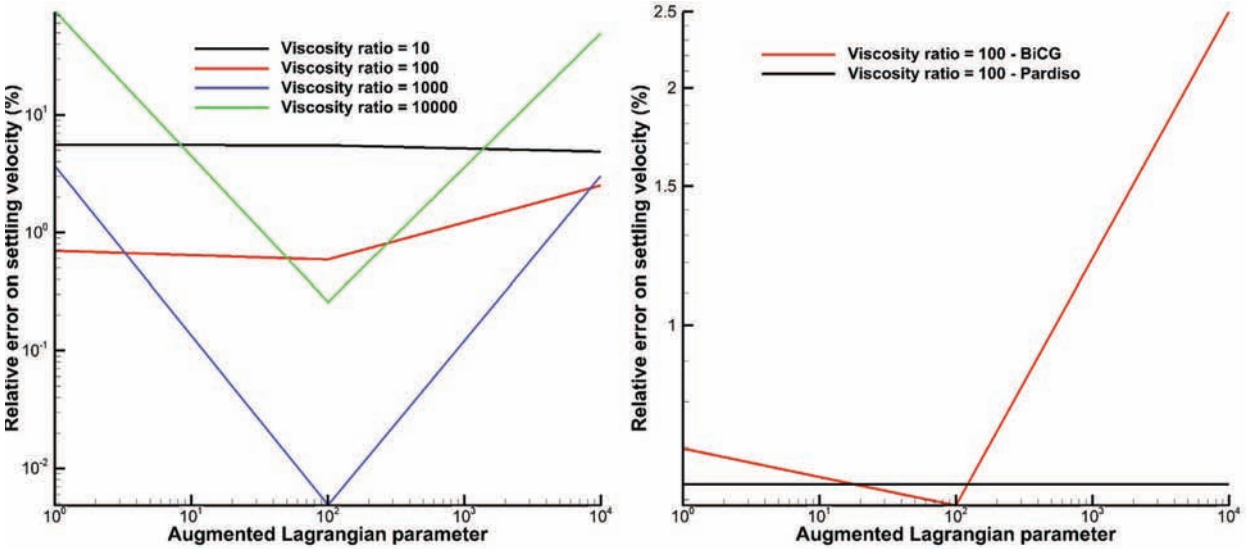


Fig. 10. Comparison of relative errors on settling velocity: left, results obtained with the iterative solver for various viscosity ratios and augmented Lagrangian parameter $\mathcal{K}$ and right, comparison of PARDISO and BiCGSTAB II for a viscosity ratio of 100.

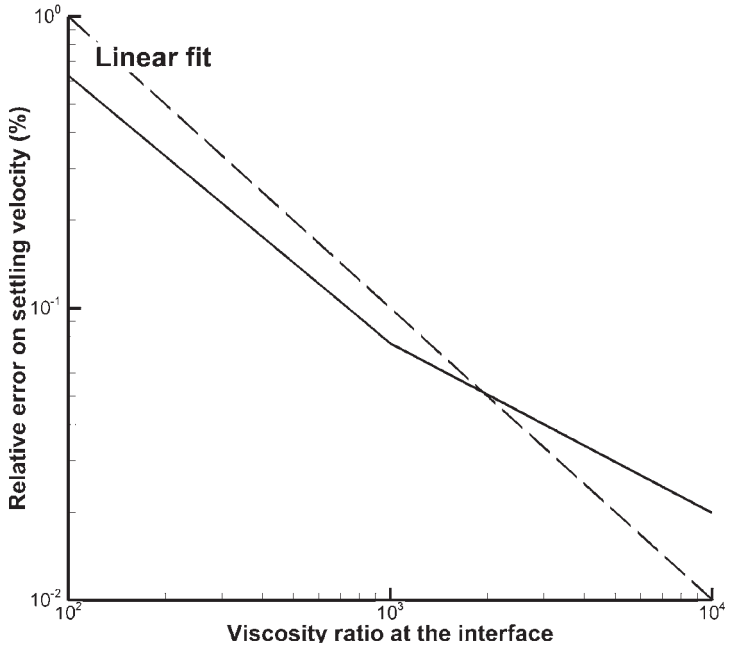


Fig. 11. Sensitivity of the relative error on U_∞ obtained with the PARDISO solver for various viscosity ratios.

3.1.2. Convergence study

A space convergence study is carried out for estimating if a high order (second order can be expected) convergence rate of the ITPM is reached and if it is consistent with the second order of the centered schemes used to discretize the fluxes in the finite volume method. The following numerical parameters are considered for the simulations: a PARDISO solver is utilized with Δt_2 and $\mathcal{K} = 10^8$. The effect of the viscosity ratio is estimated in the range 100 to 10 000 whereas the grids G_1 to G_5 are also considered. For a given viscosity ratio, the space convergence order α_s is calculated by means of the Richardson extrapolation method on four solutions as follows [81]:

$$\alpha_s = \frac{\ln(|\frac{|U_\infty|_{G_2} - |U_\infty|_{G_4}}{|U_\infty|_{G_3} - |U_\infty|_{G_5}}|)}{\ln(2)} \tag{55}$$

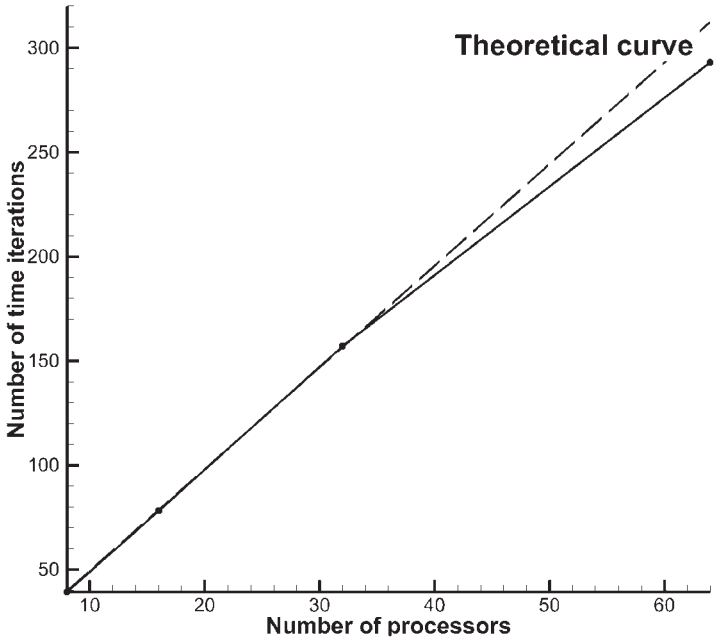


Fig. 12. Evolution of the time iterations calculated in one hour of CPU time according to the number of processors.

Table 1
Settling velocity (in $\mathrm{m\,s^{-1}}$) according to grid and viscosity ratio – the reference velocity is $-3.72753 \times 10^{-5}\ \mathrm{m\,s^{-1}}$.

Eulerian grid	Viscosity		
	ratio = 100	ratio = 1000	ratio = 10 000
G_1	-3.8189×10^{-5}	-3.7895×10^{-5}	-3.7860×10^{-5}
G_2	-3.7699×10^{-5}	-3.7448×10^{-5}	-3.7420×10^{-5}
G_3	-3.7552×10^{-5}	-3.7330×10^{-5}	-3.7306×10^{-5}
G_4	-3.7510×10^{-5}	-3.7303×10^{-5}	-3.7282×10^{-5}
G_5	-3.7497×10^{-5}	-3.7298×10^{-5}	-3.7278×10^{-5}
Convergence order α_s	1.8	2.2	2.3

where the constant 2 in relation (56) corresponds to the ratio between two consecutive numbers of grid points in each direction of space. The settling velocities of the particle for the various viscosity ratios and Eulerian grids are given in Table 1. It is observed that the finer the mesh is, the nearer is the numerical settling velocity to the analytical velocity $U_\infty = -3.72753 \times 10^{-5}\ \mathrm{m\,s^{-1}}$ from the Faxen theory. In addition, it can be concluded that increasing the viscosity ratio allows to fulfill with better accuracy the deformation free constraint in the solid particle. The resulting settling velocities are also nearer to the reference velocity for increasing viscosity ratios on a given Eulerian grid. Concerning the space convergence order, α_s slightly depends on the value of the viscosity ratio, ranging from 1.8 to 2.4 in the investigated numerical conditions. It can be concluded that a second order convergence in space is obtained whatever the viscosity ratio, as expected initially when the ITPM was designed.

To finish with, it can be important for our unsteady applications to simulate particle flows with a high order in time numerical method. The time convergence order is so calculated on G_5 with the PARDISO solver, $\mathcal{K} = 10^8$ and a viscosity ratio of 1000. The finest mesh is used in order to reduce to the maximum the space truncation error due to the space discretizations. Three time steps are considered, namely Δt_1, Δt_2 and Δt_3. The time convergence order α_t is estimated with a Richardson extrapolation on three solutions which reads

$$\alpha_t = \frac{\ln(|\frac{|U_\infty|_{\Delta t_1} - |U_\infty|_{\Delta t_2}}{|U_\infty|_{\Delta t_2} - |U_\infty|_{\Delta t_3}}|)}{\ln(10)} \tag{56}$$

The results are presented in Table 2. A second order convergence in time is obtained as for the space convergence order.

3.2. Sedimentation

The numerical simulation of the settling of a spherical particle for various Reynolds numbers is considered under the experimental conditions of [82]. Compared to the Faxen test case where $Re \ll 1$, the interest of the present configuration

Table 2
Settling velocity according to time step – the reference velocity is -3.72753×10^{-5} m.s^{-1}.

Δt_1	Δt_2	Δt_3	Convergence order α_t
-3.7615×10^{-5}	-3.7298×10^{-5}	-3.7297×10^{-5}	2.1

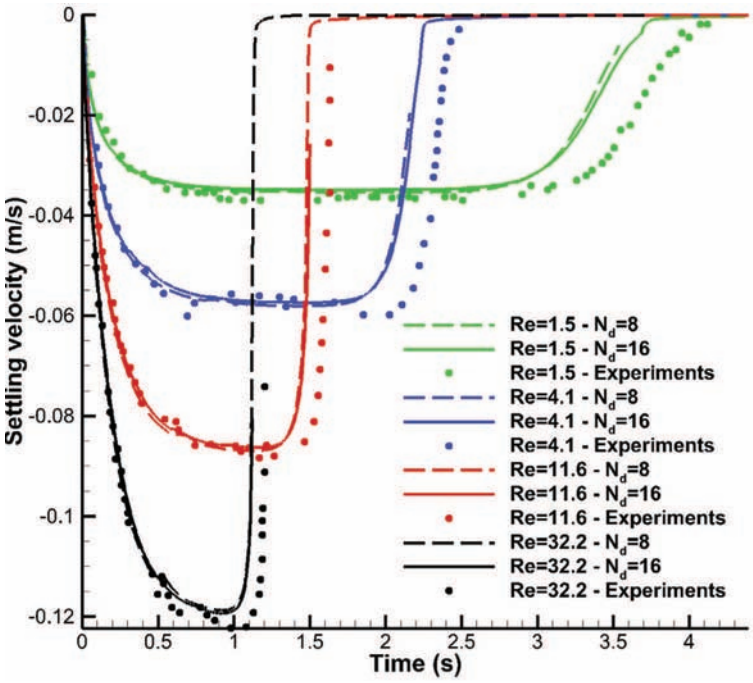


Fig. 13. Settling velocity over time for the test case of [82] – long dashed line is associated to $N_d = 8$, straight line to $N_d = 16$ and symbols to experiments [82]. Green, blue, red and black colors are related respectively to $Re = 1.5$, $Re = 4.1$, $Re = 11.6$ and $Re = 32.2$. (For interpretation of the references to color in this figure, the reader is referred to the web version of this article.)

is to investigate a particle flow in which inertial effects exist and also to compare numerical results to measurements. This problem has already been simulated by other authors with a first order penalty method [37], a Boltzmann approach [37,82], a fractional step fully resolved simulation technique [83] or an immersed boundary method [84]. The numerical parameters used in this section are a penalty viscosity 100 times larger than the fluid viscosity, 25 virtual particles per direction, viscous law NVL3, $\mathcal{K} = 100$ and an iterative solver.

The definition sketch of the particle sedimentation have been presented into details in [82]. A single spherical particle is released without initial velocity in a parallelepiped box and it reaches a limit sedimentation velocity after a characteristic time. The Reynolds 1.5, 4.1, 11.6 and 32.2 are considered here. Results in terms of settling velocity over time are reported in Fig. 13 according to the number of Eulerian grid cells for a particle diameter $N_d = D_p/\Delta x$. The simulated velocities are compared to the measurements. It can be observed that the unsteady behavior of the particle velocity as well as the limit settling velocity are nicely recovered by the simulations for all investigated Reynolds numbers. After a certain time, the numerical velocity tends to zero when the particle reaches the bottom of the tank whereas this deceleration is measured later in the experiments. These differences have previously been obtained by other authors [37,84] whereas these discrepancies are not reported in the works of [82,83]. It seems that the initial position of the particle is not exactly the same in our simulations than in the reference experiments. However, the acceleration of the particle as well as the settling velocity are correct and weakly dependent on the number of Eulerian grid cell used to simulate the problem, which is an important feature of the ITPM approach as three-dimensional simulations of finite size particles are limited by the number of flow grid cells that can be investigated in real particle flow problems.

3.3. Rotating particle

The previous test cases have demonstrated that the ITPM allows for solving a particle flow by considering the Navier–Stokes equations in the fluid and solid zones of the problem. The particle motion can be split into two constant velocity components, related to translation and angular rotation. Each particle trajectory is computed as explained in Section 2.4.1 by means of the translation velocity of the sphere barycenter. This computation is used to update the particle positions and also to build the four-way coupling force in multiple particle configurations. In this approach, as soon as the particle shape

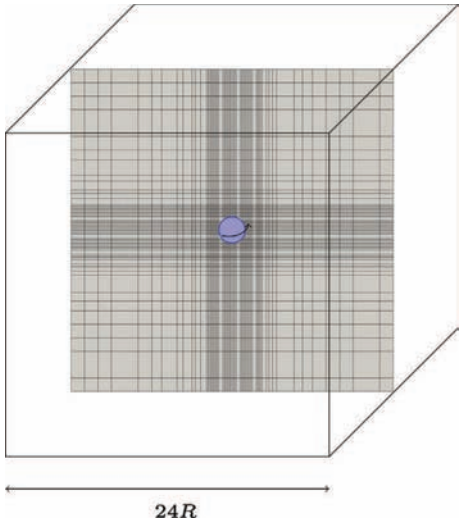


Fig. 14. Typical Eulerian grid used to simulate the rotation of a particle in a box with $N_d = 20$.

is spherical, the rotation velocity is not required. Although the angular velocity is not necessary to our method, it can be calculated as explained in Section 2.4.1. The angular velocity can be useful to understand the particle–fluid interactions. If a friction model between particles is implemented, the collision torque will be deduced from the angular velocity. A specific test case is considered in this section to validate both the ITPM method when particles rotate and the computation of angular velocities.

The flow generated by a rotating particle has been studied since the beginning of the modern fluid mechanic science [85]. When the flow becomes steady and the angular velocity of the particle remains constant, the torque exerted by the fluid on the particle have the same magnitude as the torque necessary to maintain the angular velocity. If a buoyant particle surrounded by an incompressible fluid is considered in a large fluid container, the angular velocity of the particle ω depends only on the fluid and solid densities, the fluid dynamic viscosity and the torque T exerted on the particle. The Vaschy–Buckingham π theorem shows that the problem can be reduced to a relation between the angular Reynolds number ($Re_\omega = \frac{R^2\omega\rho_f}{\mu_f}$) and the dimensionless torque ($M = \frac{2T}{\rho R^5\omega^2}$). The analytical study carried out by [86] shows that for small Re_ω, the relation between those two dimensionless numbers is $Re_\omega = \frac{16\pi}{M}$. Since, many studies have been achieved using powers of the Reynolds number [87] for finite Re numbers conditions. The retained solution is: $Re_\omega = 2.38 \times 10^{-2}\ \mathrm{M}^2$. In order to know the evolution from low to larger Reynolds numbers, two reference solutions can be considered: the first is the experiment of [88] and the second the calculations provided by [87].

The flow around the particle can be split into two contributions:

- An azimuthal velocity that decreases with the distance to the particle.
- A recirculation flow occurring near the meridian of the particle due to the centrifugal force. This flow contribution reaches back the particle near its rotation axis.

An isolated particle is considered in a box full of a viscous fluid. As previously explained, only two parameters characterize the problem, the Reynolds number and the dimensionless torque. In the present simulations, the particle radius and its density are fixed to unity. In order to limit boundary effects on the particle, the box width is taken 24 times the particle radius. This value was proposed by [89].

In order to investigate a parametric study without introducing specific numerical parameters, several cases are built to maintain the angular velocity near the unity. All parameters are fixed except:

- The viscosity, $\mu = 10^n$, with $n \in \{0, -\frac{1}{2}, -1, -\frac{3}{2}, -2, -\frac{5}{2}, -3\}$.
- The torque, that is based on the viscosity $T = 8\pi\mu R^3$. This formula respects the constraint ω equal to the unity when the Lamb law [86] is valid, *i.e.* for low Reynolds numbers.

The translation of the particle is not activated. Some tests with a free particle have been carried out and no major differences were noticed except for the lowest viscosities for which the particle position becomes unstable during time. An exponential grid has been used in each direction to concentrate calculation efforts in the vicinity of the particle, as illustrated in Fig. 14. A numerical parametric study has been achieved with 10, 20 and 40 Eulerian grid points per particle diameter N_d and time steps of 0.1, 0.05 and 0.025 s respectively. Other numerical parameters are viscous law NVL3, $\mathcal{K} = 100$ and viscous ratio of 100.

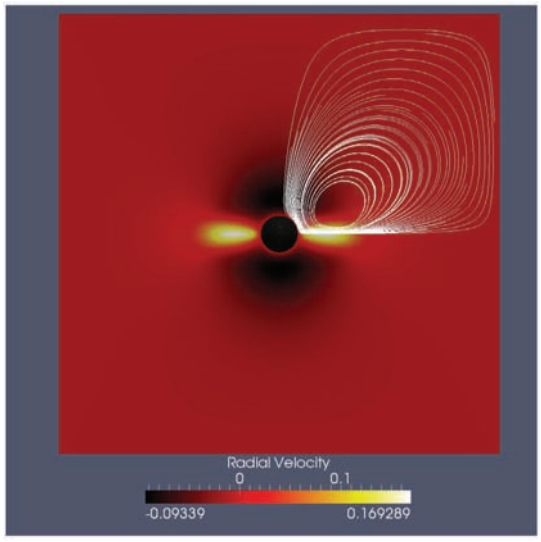


Fig. 15. Radial velocity magnitudes and streamlines in a slice for the case $\mu = 10^{-2}$ Pa s.

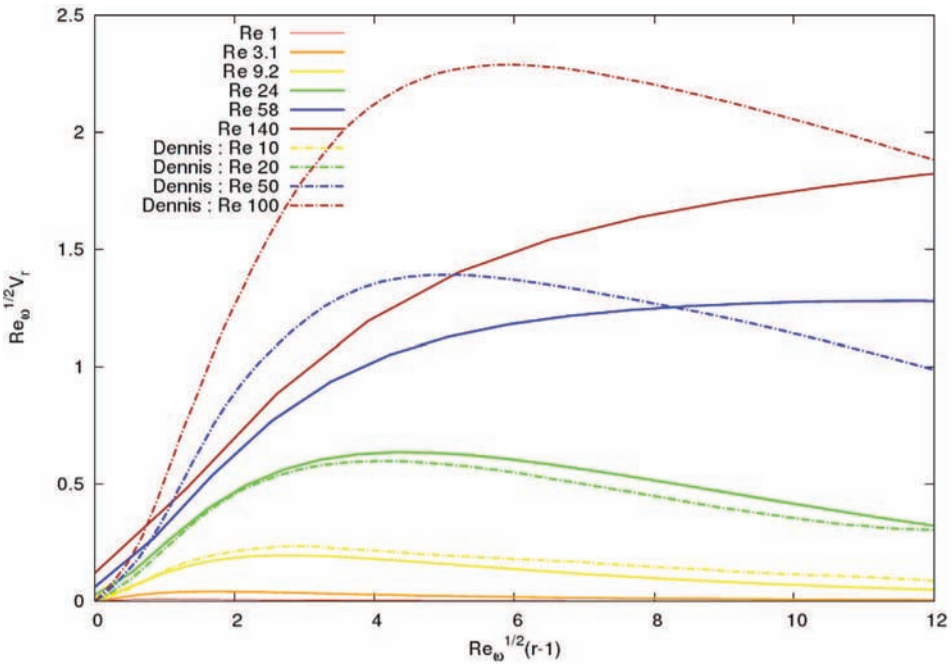


Fig. 16. Radial velocity at the meridian.

The fluid velocity is initialized with the analytical solution for Stokes flow:

$$\mathbf{u}(t=0) = \frac{R^3\omega}{r^2}\mathbf{n}_\sigma \tag{57}$$

where r is the spherical radial coordinate and $\mathbf{n}_\sigma$ the angular vector direction. In the reference article [87], the angular velocity is imposed as a boundary condition. Then, a study of the steady flow around the particle is carried out, the torque being computed from the flow. On the contrary, with the ITPM method, the torque is imposed, as the particle–fluid interface is not supported by mesh points in the 1-fluid approach, and the angular velocity is deduced from simulations. Fig. 15 illustrates the radial velocity around the particle. The lines represent the stream function of the velocity projected in a plane perpendicular to the particle shape.

The simulated flow can be compared with that presented by [87]. The comparison of radial velocity at the meridian of the particle is presented for different Navier–Stokes numbers in Fig. 16. For $Re < 25$ the results agree nicely. For higher Reynolds,

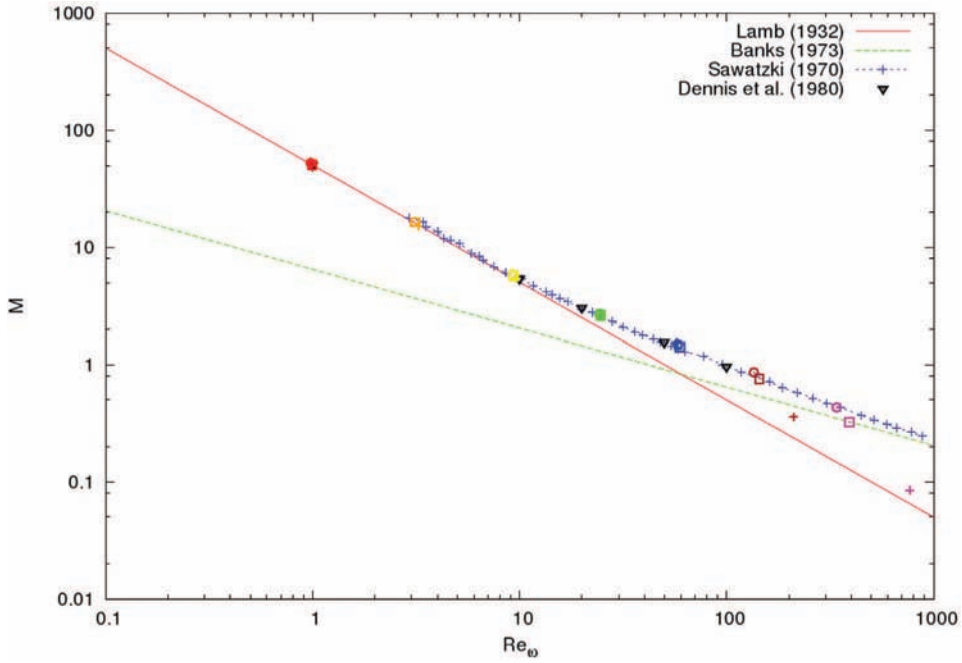


Fig. 17. Relation between the Reynolds number and the dimensionless torque. Lines correspond to references cited below. Symbols correspond to actual for different refinements (cross, circle and square for 10, 20 and 40 nodes per diameter). Colors (red, orange, yellow, green, blue, magenta and pink) are respectively for $\mu = 10^b$, $b = \{0, 0.5, \ldots, 3\}$. (For interpretation of the references to color in this figure, the reader is referred to the web version of this article.)

the solutions exhibit noticeable differences. These differences can be explained by the different boundary conditions used in the two approaches. However, even if the ITPM flow seems to disagree with the solution proposed by [87], the relation between the Reynolds number Re_ω and the dimensionless torque is respected in our approach. As was explained at the beginning of this section, a relation exists between the Reynolds number and the dimensionless torque. In order to calculate the angular velocity, the torque is maintained. When the angular velocity remains constant, the simulations are stopped and the angular velocities evaluated.

To finish with, Fig. 17 shows the relation between the Reynolds and Torque numbers opposed to the theoretical correlations and experiments of [86–88,90]. The various colors are for different viscosities whereas each symbol corresponds to a specific grid refinement. The numerical results show that for low Reynolds numbers the rotation is well represented on coarse and fine meshes while when the Reynolds number is important, a high grid resolution is necessary to obtain correct results. It has been demonstrated that the ITPM approach reproduces the rotation correctly for a wide range of angular Reynolds numbers. In the cases presented after, this Reynolds number will be in the range where the ITPM agrees with the physics, *i.e.* for $8 \leqslant N_d \leqslant 16$. The torque distributed inside the particle volume seems to be a correct solution for future implementations of rotational contributions such as the Coulomb forces.

3.4. Particle in a Poiseuille flow

A particle surrounded by a shear flow is now considered. It is moved by the mean velocity and is rotated by the shear. This typical flow configuration is present in most of real particle flows. In the cases presented in Sections 3.2 and 3.3, the displacement and the rotation or the particle was induced by a volume force, namely gravity or torque. It is necessary to verify that the ITPM is able to reproduce also the surface forces induced by a flow on a particle. The chosen problem permits to validate the displacement and rotation induced by the fluid on the solid sphere.

This configuration presents three major advantages: the particle will be displaced and rotated by the flow, the case is well documented and some two-dimensional solutions exist. This case was first studied by Segré and Silberberg [91–93]. They noticed that when a particle is placed in a tube submitted to a Poiseuille flow, the solid sphere reaches an equilibrium position after a certain time. This position was in their case 0.6 times the tube radius. This equilibrium position is associated to an angular velocity and a translation velocity along the axis of the tube. Many studies followed up the study made by Segré and Silberberg. The purpose being to understand the dependency of the equilibrium position on various parameters such as the Reynolds number or the density ratios. The influence of the pattern of the tube was also studied. Differences were noticed between circular tubes, squared tubes and a planar Poiseuille flow [94]. Matas [95] summarizes many of those cases in his introduction.

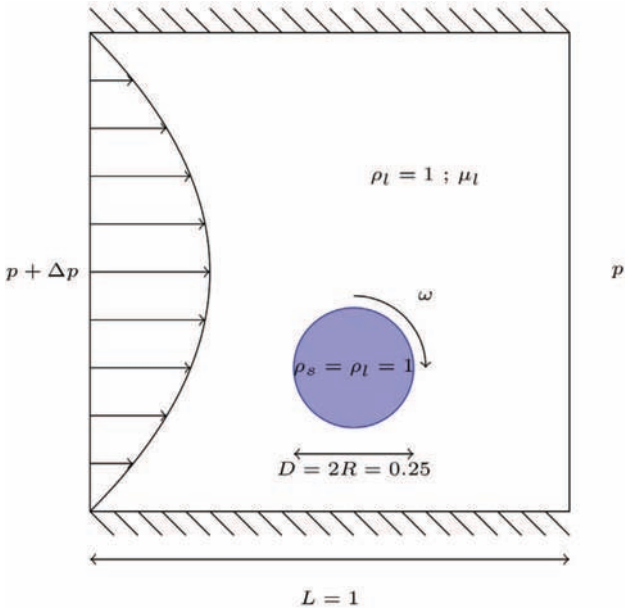


Fig. 18. Definition sketch of the Poiseuille flow corresponding to the first configuration of [100].

The motion of a particle in a Poiseuille flow is present in many domains: andrology [96], chemical engineering [97], aerodynamics, rheology [98], which explains that it is very well documented. The configuration under consideration in two dimensions is the case proposed by [99] which was simulated by [100]. A two-dimensional particle is placed in a staggered flow. The domain is a square for which the bottom and floor boundaries are walls and the left and right boundaries are periodic. The Poiseuille flow is forced by a pressure gradient. The liquid and the particle densities are fixed and equal, $\rho_l = \rho_s = 1\ \mathrm{kg\,m^{-3}}$. The length of the box is the unity too, $L = 1$ m. The particle radius is $R = L/8 = 0.125$ m. The initial vertical position of the particle is $y = 0.4$ m. The definition sketch describing this configuration is presented in Fig. 18 and in [100] concerning their first case of Table I, p. 269. The liquid viscosity is $\mu_l = 3.250 \times 10^{-3}$ Pa s whereas the pressure difference Δp in the horizontal direction is chosen equal to 1.763×10^{-3} Pa.

The different numerical viscous laws NVL1 to NVL4 are compared here in order to discriminate the best choice for future simulations. A comparison concerning the vertical position Y_p and horizontal velocity component U_p of the particle are presented in Fig. 19 after an equilibrium position is reached. The reference values obtained by [99] are $Y_p = 0.2745$ m and $U_p = 0.04137\ \mathrm{m\,s^{-1}}$ whereas results of [100] were $Y_p = 0.2732$ m and $U_p = 0.04155\ \mathrm{m\,s^{-1}}$. For $N_d = 25$, $\mu_s = 1$ Pa s and $\mathcal{K} = 100$, it can be observed that the discontinuous and arithmetic numerical viscous laws NVL1 and NVL2 involve asymptotic values for $Y_p \approx 0.3$ m and $0.044 \leqslant U_p \leqslant 0.045\ \mathrm{m\,s^{-1}}$, which is not correct. Moreover, when the particle crosses a grid cell, a discontinuity is observed in the velocity for these numerical viscous laws. In addition, discontinuities are observed on the velocity history which is not a physical behavior. The two other numerical viscous laws does not produce velocity discontinuities, $Y_p = 0.27$ m being better with NVL3 while $U_p = 0.043\ \mathrm{m\,s^{-1}}$ is better with NVL4. In the rest of the article, we have chosen to use NVL3. Concerning space convergence orders, a Richarson analysis have been investigated as in the previous sections. Orders 1.83, 1.83 and 1.64 have been obtained respectively for translation velocity, vertical position and rotation velocity of the particle. A time step sensitivity study is also provided concerning Y_p after a stabilized regime is reached. The CFL number based on the constant space step and reference particle velocity is investigated. Results are proposed in Fig. 20. It can be concluded that the ITPM approach is mainly independent on the choice of the time step as soon as the CFL number is lower than 0.5. The reason is that for a time step such as CFL is less than 0.5, a given particle does not cross more than half an Eulerian grid cell in one time iteration. So the time splitting error due to the decoupling between particle advection and pressure-velocity solving becomes negligible for these time steps.

4. Simulation of dense particle-laden flows

4.1. Motivations

Particles and processes involving particles are of paramount importance in the chemical and applied industries. As an illustration of the potential brought by the ITPM and more generally by the DNS of finite size particle simulations, the flow across fixed and circulating fluidized beds is investigated in this section. Fluidized beds are widely employed in industrial operations, ranging from the pharmaceutical and food industry, to processes such as catalytic cracking of petroleum, combustion and biomass gasification. The success of fluidized bed processes is due to their excellent heat and mass transfer characteristics. Although rather simple in its conception, the application of a fluidized process still faces some challenges:

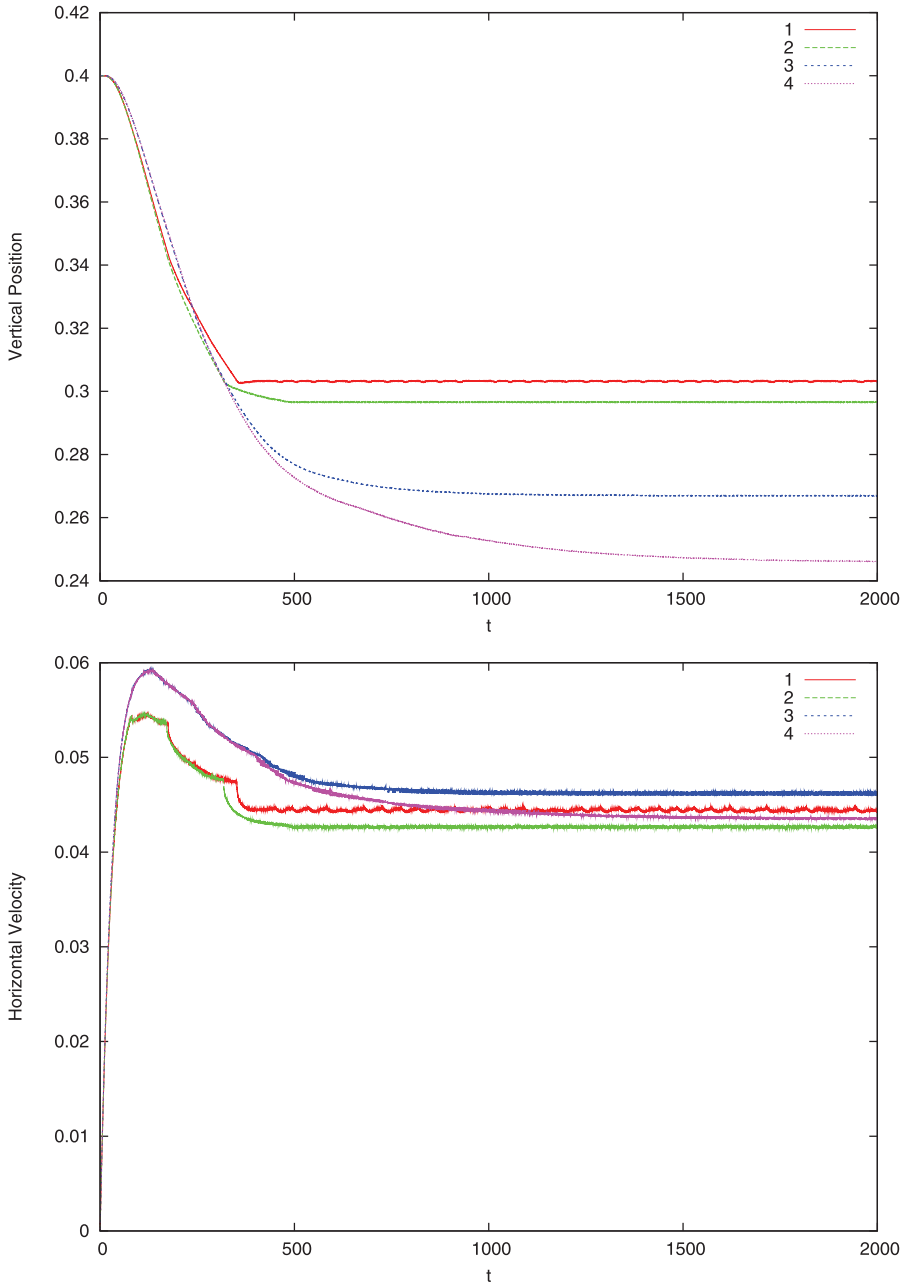


Fig. 19. Time evolution of the vertical position (top) and horizontal velocity component (bottom) of the particle for viscous laws NVL1 (red line), NVL2 (green line), NVL3 (blue line) and NVL4 (pink line). (For interpretation of the references to color in this figure, the reader is referred to the web version of this article.)

a sound understanding of the mechanisms governing the complex flow phenomena involved in a fluidized bed still remains an open technical and scientific issue.

Several modeling issues can be investigated to simulate dense particle flows as fluidized beds. On a macroscopic point of view, Eulerian–Eulerian models based on the Kinetic Theory of Granular Flows (KTGF) can be used to simulate the large scales of the flow, the particle being assumed to be of small size compared to the characteristic scales of the flow. They are represented through a diffuse volume fraction. The work of [102] in this field has allowed to recover good results concerning granular pressure and concentration waves. The main drawback of these models is associated to the requirement of defining *a priori* macroscopic particle parameters such as the drag force. The models have been mainly used in two-dimensions. Under the same scale separation assumption concerning the size of the particles, Eulerian–Lagrangian models also exist [103] in which the particle are considered as force points transported by flow. One or two-way coupling models exist in order to account of the interacting between particles and the surrounding motion. This type of modeling is generally

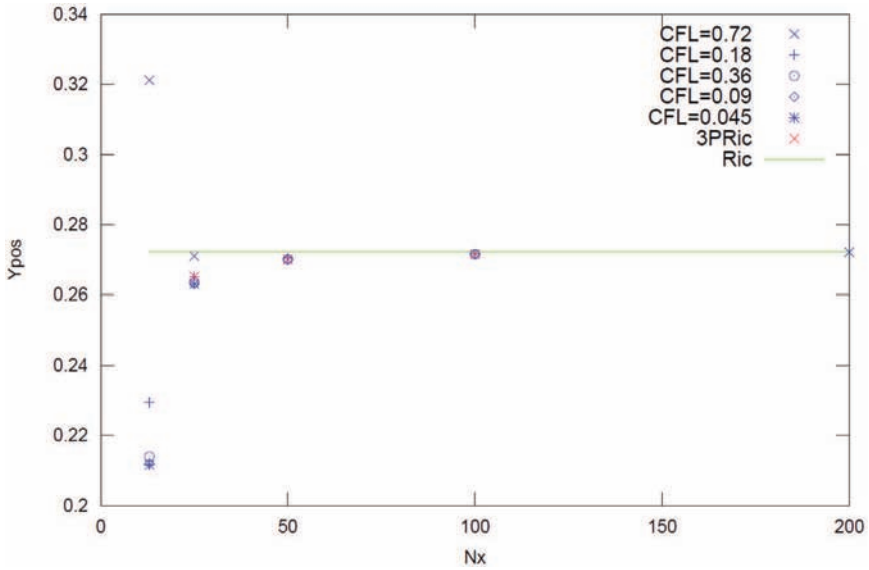


Fig. 20. Time evolution of the vertical position of the particle for various CFL numbers. The asymptotic numerical values 3PRic and Ric stands for extrapolation of Y_p through the Richardson theory [101] on 3 points (3PRic) and 4 points (Ric).

applied to gas particle fluidized beds. As for Eulerian–Eulerian approaches, it requires the *a priori* definition of interaction terms concerning the drag force or particle collisions.

The constant increase of the power brought by supercomputers and the development of new numerical methods have allowed to carry out in rare research works direct numerical simulation DNS of real fluidized beds with thousands of particles. To the knowledge of the authors, only three publications exist in the field of DNS of mono-dispersed particles fluidized by a liquid, all being investigated on Eulerian fixed grids: the distributed Lagrangian method of [35] which is validated and compared to dedicated experiments, the lattice Boltzmann method of [104] which is used to simulate wave instabilities in fluidized beds and the present work which uses fictitious domain approaches and penalty methods [10,34]. The interest of these unsteady and small scale simulations of resolved scale particles, *i.e.* the grid space scale is smaller than the particle diameter, is to enable to model both the fluid and particle motions in a coupled way without considering any assumption on the particle size nor on any space scale separation. The domain of interest of the DNS is the particle motions in which the size of the particle lies in the range of the small flow scale, typically the Kolmogorov scale for turbulent flows, and the integral scale. The present section aims at presenting for the analysis of a real DNS of a fluidized bed in terms of instantaneous local flow motion, statistical variables required in KTGF based models, time spectra of particle velocities or solid fractions and averaged quantities. These DNS are a good illustration of the potential brought by the numerical methods presented in the present article.

4.2. Two-dimensional flow across a fixed array of cylinders

As a preliminary use of the ITPM when dense particle flows are considered, the flow over a fixed array of cylinders is first simulated, in a geometry similar to the one utilized in the next section concerning a real circulating fluidized bed. The goal is to evaluate the accuracy and consistency of the ITPM when pressure and drag interaction are involved between particles. A set of cylinders of diameter $d_p = 0.006$ m is placed in a two-dimensional tank of height $H = 0.64$ m full of potassium thiocyanate KSCN (see next section for density ρ_l and viscosity μ_l of this KSCN fluid). The height of the fixed bed is 0.47 m, as illustrated in Fig. 21. The solid fraction α is equal to 0.1. A fluidization velocity U_0 of 0.12 m s^{-1} is imposed at the bottom boundary of the simulation domain while wall conditions are chosen on left and right boundaries and a Neumann condition on the top of the tank. The parameters of the ITPM are fixed to a penalty solid viscosity 100 times larger than μ_l and $\mathcal{K} = 100$. Thanks to a penalty method, the velocity at the center of the particles is imposed to be zero in order to maintain a fixed bed. Three grids $G1$, $G2$ and $G3$, containing respectively 160×1280, 320×2560 and 640×5120 cells, are also considered for a space convergence study. The typical pressure and velocity fields obtained when the fluid interacts with the fixed bed are proposed in Fig. 21. It is observed that a global linear pressure variation is established vertically inside the bed while locally, recirculating patterns are attached to the particles. In Table 3 are presented the vertical pressure discharges ∇p_α according to the grid used and also according to the numerical diameter d_n of the particle used to define the penalty viscosity. The values of the pressure discharge can be compared to the theoretical pressure discharge obtained by equating the different forces acting on the particles:

$$\nabla p_\alpha = -\alpha(1-\alpha)^{-Ndim-3}\rho_l \frac{18\nu_l}{d_p^2}\left[1 + 0.15\,Re_p^{0.687}\right]U_0 \tag{58}$$

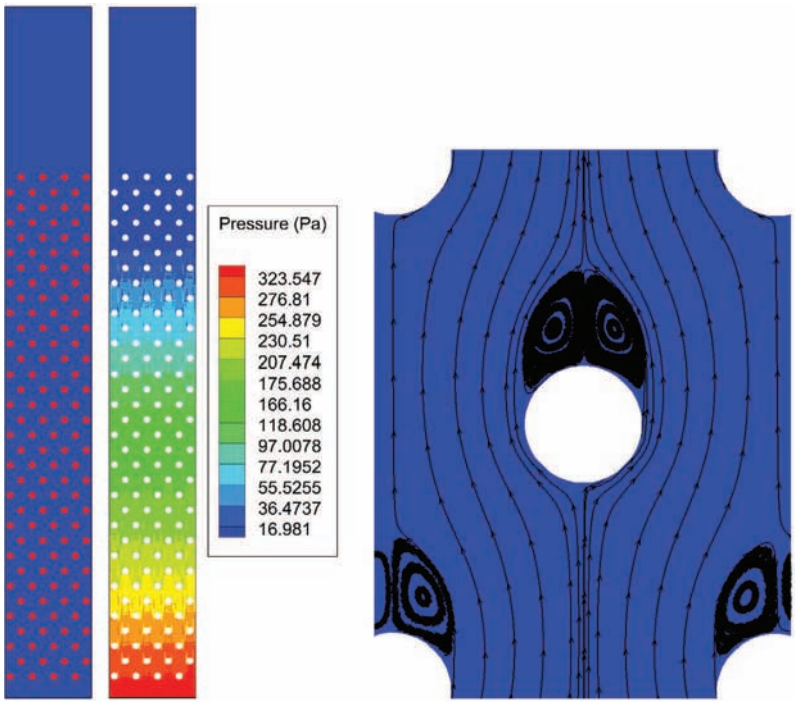


Fig. 21. Two-dimensional flow across a fixed array of cylinders – the positions of the cylinders in the tank (left), the macroscopic pressure across the fixed bed (middle), and a zoom on the velocity field in the vicinity of a particle (right) are presented.

Table 3
Pressure discharges for the flow across a fixed bed of circular particles.

Grid	$d_n = d_p$	$d_n = d_p - \Delta x/2$	$d_n = d_p - \Delta x$
$G1$	971 $\mathrm{Pa\,m^{-1}}$	794 $\mathrm{Pa\,m^{-1}}$	578 $\mathrm{Pa\,m^{-1}}$
$G2$	483 $\mathrm{Pa\,m^{-1}}$	416 $\mathrm{Pa\,m^{-1}}$	367 $\mathrm{Pa\,m^{-1}}$
$G3$	320 $\mathrm{Pa\,m^{-1}}$	340 $\mathrm{Pa\,m^{-1}}$	280 $\mathrm{Pa\,m^{-1}}$

where Re_p is the particle Reynolds number and $Ndim$ is the number of space dimensions. In our configuration, $\nabla p_{0.1} = 319\ \mathrm{Pa\,m^{-1}}$. It is observed that when $d_n = d_p$, the numerical pressure discharge across the fixed bed converges to the expected theoretical value. However, good results are obtained only if at least 24 cells along a particle diameter are considered (grid G_3). Such a resolution cannot be implemented for three-dimensional particle flows. On coarser grids, the shape of the particle tends to be overestimated, and so the corresponding drag effects, due to the definition of the penalty viscosity after the exact shape of the particle is projected onto the Eulerian Navier–Stokes grid. To avoid this drawback, the numerical radius of the particle d_n considered for the definition of the penalty viscosity has been reduced by $\Delta x/2$ and Δx. In this way, a better pressure discharge has been obtained on coarser grids. This procedure has been used in the next section to simulate circulating fluidized beds.

4.3. Simulation of a circulating fluidized bed

4.3.1. Presentation of the fluidized bed

The fluidized bed chosen for the simulations is taken from the experiments of Aguilar Corona [105]. In a cylinder of 0.64 m height and 0.08 m diameter, 2133 pyrex particles are fluidized by the circulation of potassium thiocyanate KSCN at various fluidization velocities. The diameter of the particles is 0.006 m and the simulated fluidization velocity is $0.12\ \mathrm{m\,s^{-1}}$. The density of the pyrex is $\rho_s = 2230\ \mathrm{kg\,m^{-3}}$ whereas the density ρ_l and the dynamic viscosity μ_l of the KSCN are $1400\ \mathrm{kg\,m^{-3}}$ and 3.8×10^{-3} Pa s. For the chosen particles in KSCN, the terminal settling velocity is equal to $0.226\ \mathrm{m\,s^{-1}}$, the particle Reynolds number based on this velocity is equal to 530 and the Stokes number is 0.8.

Concerning the DNS of particles, a parallelepiped box of dimensions 8 cm × 8 cm × 64 cm is used with a grid mesh containing 160 × 160 × 1280 cells. With such a grid resolution, nearly 12 cell length Δx per particle diameter is achieved. The other numerical parameters used are a penalty solid viscosity 100 times larger than μ_l and $\mathcal{K} = 100$. The cylinder is represented numerically with a Darcy penalty method [43]. The method consists in adding a Darcy term $\frac{\mu}{K}\mathbf{u}$ in the momentum equations. By taking a permeability tending to zero in the cells being outside the cylinder, a null velocity is imposed. A permeability of $10^{-40}\ \mathrm{m^2}$ is used in the simulations in the solid parts outside the cylindrical vein. The

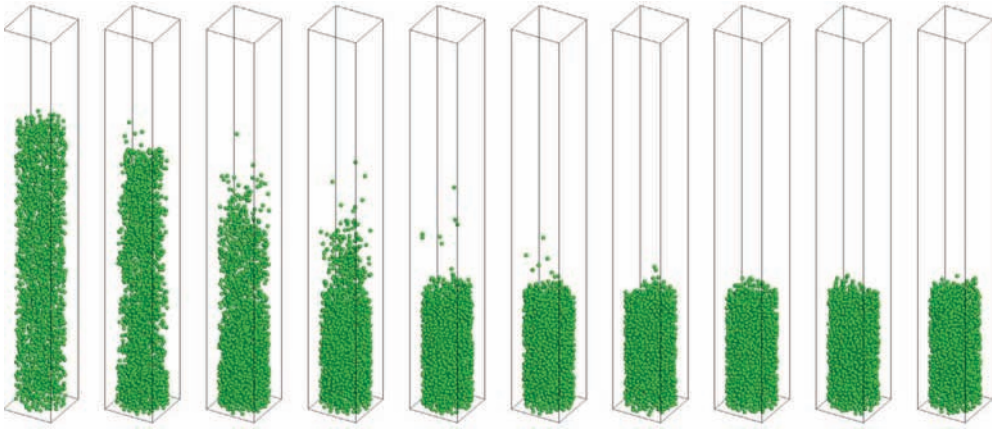


Fig. 22. Three-dimensional view of the particles inside the fluidized bed – from left to right, $t = 1$, 2, 3, 4, 5, 6, 7, 8, 9 and 10 s.

permeability is 10^{40} m^2 elsewhere such that the effect of the Darcy term vanishes in the fluid and particles. The rebound of particles on the walls of the cylindrical tank is treated as a rebound between two particles. The simulations are conducted during a total physical time of 10 s with a numerical time step of $\Delta t = 0.001$ s. They are run on 512 Intel Quad-Core processors of the CICT computing center of Toulouse and CINES computing center of the French Ministry of Research. In the present simulation, 33 millions of grid cells are used in the whole numerical domain, which lead to blocs of 64 000 cells on 512 processors. In this way, the fluidized bed simulation belongs to the range of speed-up 1 for the ITPM, as demonstrated before for a two-dimensional case. In three dimensions, the speed-up equal to one zone is maintained, for a given number of grid points, for a larger number of processors than in two dimensions. The CPU time for simulating 10 s of physical time is 25 days. The initial distribution of the particle position is randomized in the first 0.47 m of the fluidization cylinder, which corresponds to an average solid fraction of 0.1. For the tensorial penalty of the particles, a reduced diameter of the spheres $d_p - \Delta x$ is considered so as to obtain a correct effective drag force exerted by the fluid on the particles (see previous Section 4.2). Indeed, the projected shape of the spheres is different from the real one as explained in Section 2.3.1. The real particle shape is considered for the definition of the solid density and the treatment of the collisions between the particles.

4.3.2. Macroscopic results

The macroscopic characteristics of the fluidized bed are first presented in order to validate the global interaction between the 2133 particles and the carrier fluid. The typical particle structures are illustrated in Fig. 22 over time. It is observed that from $t = 0$ s to 6 s, a packing occurs as the initial particle concentration α, *i.e.* $\alpha = 0.1$, is small compared to the fluidization velocity of 0.12 m s^{-1}. After 6 s, the fluidization regime is reached and the average bed height and resulting solid concentration in the vertical cylinder remain almost constant over time, as described in Fig. 23. The average numerical solid concentration α_n so obtained is 0.24. For the chosen operating conditions, this value of α_n can be compared to the reference experimental correlation of Richardson and Zaki [101] which reads

$$\alpha_{RZ} = 1 - \left(\frac{U_0}{U_t}\right)^{1/2.41} \tag{59}$$

where the parameter 2.41 is correct for Reynolds numbers Re_t based on the settling particle velocity larger than 500. In our configuration, $Re_t = 530$. Concerning the fluidization velocity U_0 and the settling particle velocity U_t, the values of 0.12 m s^{-1} and 0.226 m s^{-1} are measured in the experiments of [105]. Finally, it is found that $\alpha_{RZ} = 0.231$. A very good agreement is found between experiments and numerical solutions. This comparison validates the use of two numerical radii for the particles, one for the definition of the density and the treatment of the collisions and the other for the penalty viscosity. A correct global equilibrium between the gravity and drag forces is so obtained.

In a vertical slice passing by the axis of the cylinder, the velocity field and pressure distributions are presented in Fig. 24. It can be remarked that even after 10 000 calculation iterations, the shape of the particles remains spherical thanks to the Lagrangian VOF method. Strong acceleration zones are also noticed in the carrier fluid as well as recirculation patterns, following the instantaneous positions of the particles. The macroscopic vertical pressure gradient estimated inside the bed after 10 s is the following

$$\nabla p \approx \frac{\Delta p}{H} = \frac{3000}{0.2} = 15\,000 \text{ Pa m}^{-1} \tag{60}$$

where $H = 0.2$ m is the average height of the fluidized bed. The vertical pressure distribution is almost linear, as in a fixed bed.

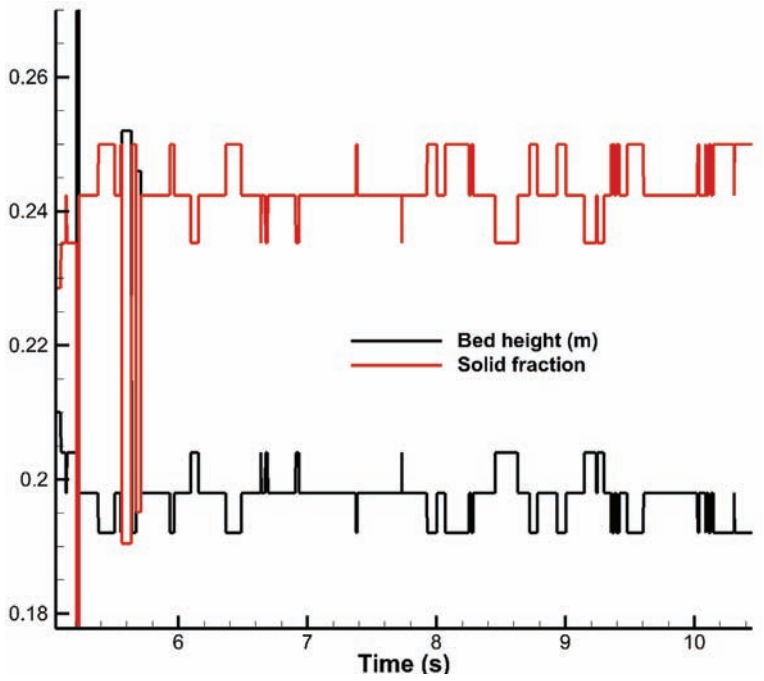


Fig. 23. Time evolution of the bed height and corresponding solid fraction over time.

Table 4
Asymptotic values of $\frac{M_{\alpha\alpha}(t)}{t}$ for each Cartesian direction.

	x-direction	y-direction	z-direction
experiments of [105] ($m^2\,s^{-1}$)	5.4×10^{-5}	5.1×10^{-5}	6.8×10^{-4}
simulations ($m^2\,s^{-1}$)	7.7×10^{-5}	8.6×10^{-5}	9.5×10^{-4}

4.3.3. Lagrangian characteristics

The first Lagrangian characteristics that can be studied are the particle velocity fluctuations over time in the fluidization regime, for $t > 6$ s. In this particular flow conditions, the mean particle positions are null as the height of the bed is constant over time. The numerically measured time averaged particle velocities are $\bar{U}_x = 7.2150 \times 10^{-5}\ \mathrm{m\,s^{-1}}$, $\bar{U}_y = 7.7822 \times 10^{-5}\ \mathrm{m\,s^{-1}}$ and $\bar{U}_z = 1.4128 \times 10^{-5}\ \mathrm{m\,s^{-1}}$ respectively in the x, y and z directions. These values are four orders of magnitude smaller than the fluidization velocity and can be considered as zero. The particle velocity fluctuations are obtained as the difference between the instantaneous values and the average one. Their average over the ensemble of the particle at each time step is plotted in Fig. 25. It is observed that these fluctuations are oscillating around zero, as expected. They are two orders of magnitude smaller than the fluidization velocity. The same particle velocity fluctuations, measured in the experiments for one tracer particle, are one order of magnitude larger than in the simulations. A statistical estimate of these fluctuations should be realized experimentally to compare them to the numerical simulations.

A last parameter of interest to feed the macroscopic Eulerian–Eulerian models devoted to fluidized beds is the autodiffusion coefficient $D_{\alpha\alpha}$. It is defined [105] according to the variance of the particle displacement $M_{\alpha\alpha} = \langle \mathbf{X}_i - \mathbf{X}_{i,0} \rangle$ as

$$D_{\alpha\alpha} = \lim_{t - t_0 \to +\infty} \frac{M_{\alpha\alpha}(t)}{t} \tag{61}$$

where $\mathbf{X}_i$ is the coordinate vector of one particle at a given time step and $\mathbf{X}_{i,0}$ is the coordinate vector of the same particle at an initial time t_0. The notation $\langle \cdot \rangle$ stands for the average over all the particles i, $i = 1..2133$. In the experiments [105], it has been demonstrated that for small time steps, a t^{-2} slope was observed for $D_{\alpha\alpha}$ whereas an asymptotic value was reached for larger times. This asymptotic value is the autodiffusion coefficient in a given direction. The curve of $\frac{M_{\alpha\alpha}(t)}{t}$ is presented in Fig. 26. The same slope as in the experiments in found numerically for small time steps. The asymptotic values obtained numerically and in the experiments for $D_{\alpha\alpha}$ are proposed in Table 4. A good agreement is found between experiments and numerical solutions, the vertical component being one order of magnitude larger than in the horizontal directions. A 30% to 40% gap is nevertheless observed between both approaches. A more accurate study should be led paying attention to experimental uncertainties.

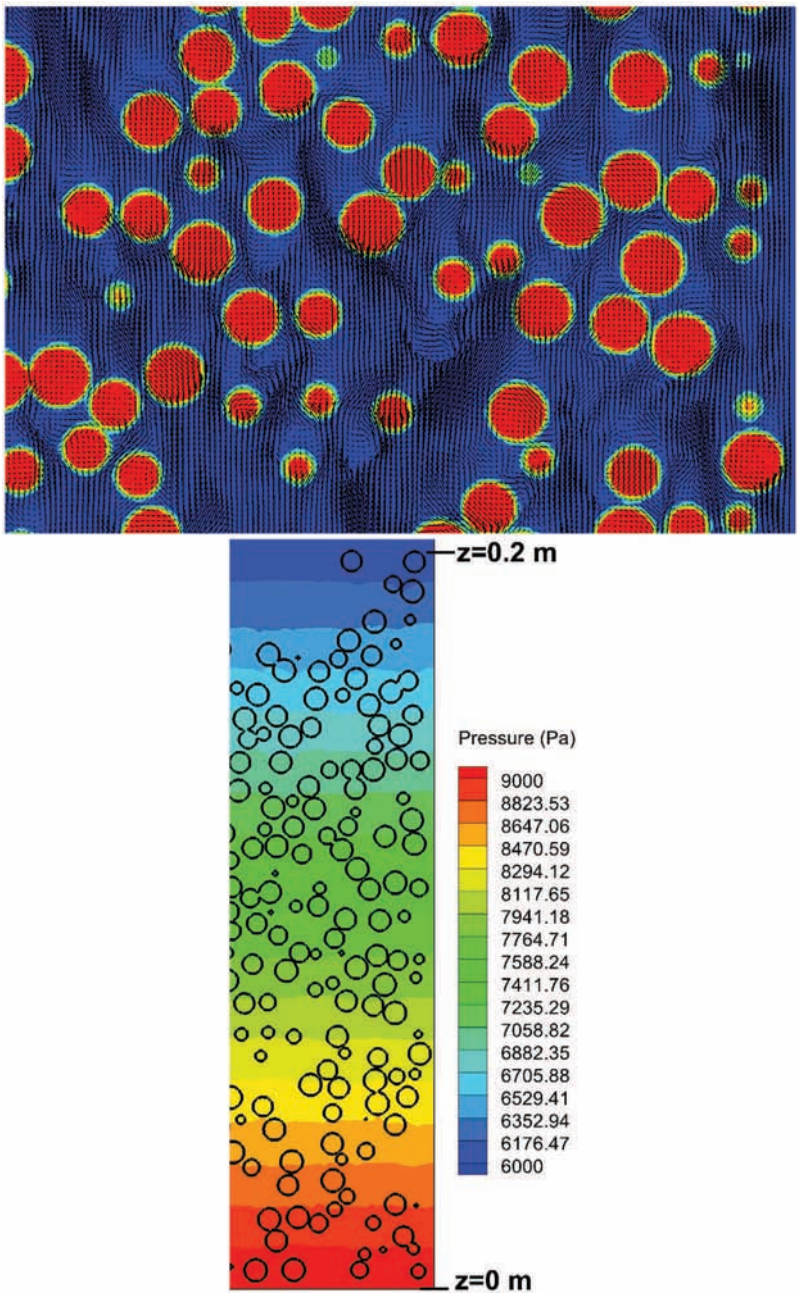


Fig. 24. Instantaneous view of the fluidized bed in a medium vertical slice at $t = 10$ s – top: particles and velocity field in a zoom – bottom: particles (lines) and pressure in the whole bed. (For interpretation of the references to color in this figure, the reader is referred to the web version of this article.)

5. Conclusion and perspectives

A fictitious domain approach based on augmented Lagrangian techniques and penalty methods has been presented for handling particulate flows of resolved scale particle. The objective was to design specific treatment of penalty Navier–Stokes equations in order to reach a second order convergence in space and time for the method. The proposed implicit tensorial penalty method uses a dual viscosity grid and a decomposition of the viscous stress tensor, together with an algebraic adaptive augmented Lagrangian method for pressure-velocity coupling, a Lagrangian Volume of Fluid–particle tracking and a four-way coupling collision model for multiple particle flows. The framework of fixed grids being considered for a simple particle tracking, a one-fluid formalism has been extended to particle flows with various numerical viscous laws being proposed.

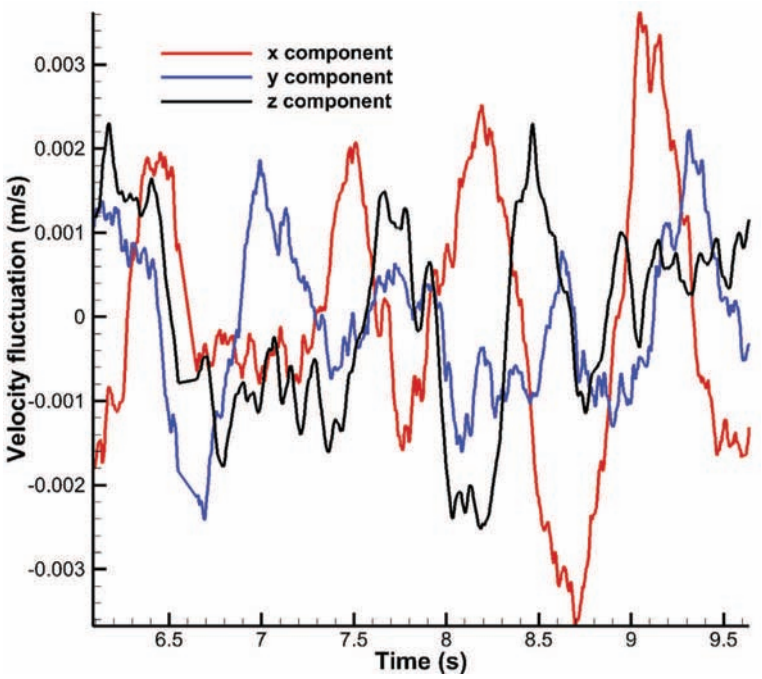


Fig. 25. Time evolution of particle velocity fluctuations.

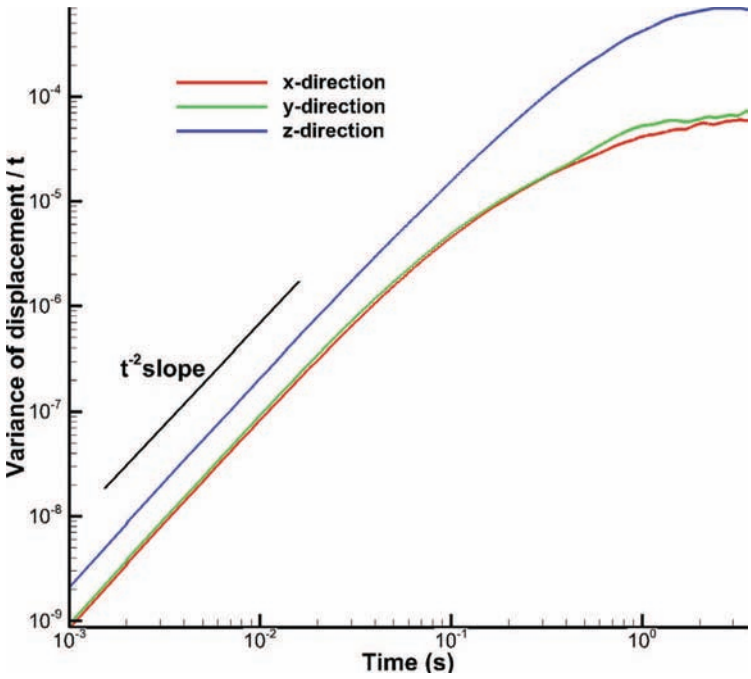


Fig. 26. Variance of the displacement of the particles $\frac{M_{\alpha\alpha}}{t}$ according to time.

A large part of the article has been devoted to validations. Complete analysis of various numerical parameters has been provided concerning the Faxen theory for a circular particle settling in Stokes flow in a 2D tank. Second order in time and space has been obtained as expected. The forced rotation of a particle interacting with a fluid, the motion of a solid sphere in a Poiseuille flow and the settling of a 3D particle in a tank. In all configurations, comparisons to experiments, theory or other numerical simulations have provided a successful validation of the ITPM with the use of few Eulerian grid cells by particle diameter. This numerical constraint is fundamental to allow for the DNS of real three-dimensional particulate flows.

The final part of the work have been concentrated on the simulation of a real fluidized bed, in order to illustrate the ability of the ITPM to deal with dense particulate flows. Again, the simulations have been favorably compared to reference experiments or theoretical results of the literature such as the fluidization velocity, variance of particle position or autodiffusion coefficient. These simulations are a first step for managing numerical experiments with the DNS of particle flows. This is now possible on massively parallel computers, as 512 processors were used in the proposed simulations of fluidized beds.

A lot of work remains to be done concerning numerical efficiency. It has been explained that the use of penalty method requires to possess efficient iterative preconditioned solvers usable on parallel architectures. In the present work, classical existing solvers have been investigated, namely the BiCGSTAB II solver, with a numerical time cost remaining important in parallel computations. A specific work will be required to design specific preconditioning to the shape of the matrix involved by the augmented Lagrangian and penalty method. Another interesting research area will be the integration of the particle tracking inside the momentum solving algorithm in order to improve the implicit character of the ITPM. Indeed, the collision force which is integrated in the Navier–Stokes equations for the four-way coupling is based on an extrapolation position of the velocity from previous time step. This force estimate could be updated directly in the solving process of the momentum equations, improving the implicit and coupled character of the particle flow. The DNS of resolved dense particle flows could also be used to simulate the behavior of particles in simple sheared flows under periodic boundary conditions. The simulated results could be compared to the reference works of Sangani et al. [106] and Abbas et al. [107].

Acknowledgements

The authors wish to thank the Midi-Pyrennées and Aquitaine Regional Council for the financial support dedicated to a PhD thesis at ONERA and IMFT and a 256-processor cluster investment, located in the TREFLE laboratory. We are grateful for access to the computational facilities of the French CINES (National Computing Center for Higher Education) and CCRT (National Computing Center of CEA) under project number x2012026115. This work was also partly granted access to the HPC resources of CALMIP under the allocation 2012-P0633. The Agence Nationale de la Recherche ANR through the Player project is associated to this work for its support of I2M and IMFT laboratories concerning the DNS of the interaction between particles and unsteady flows.

References

[1] P. Minutolo, M.V. Prati, M. Sirignano, A. D'Anna, Emission of particles from practical combustion devices burning methane/natural gas, in: European Aerosol Conference 2009, Karlsruhe, 2009.
[2] E.R. Bissell, A.K. Burnham, R.L. Braun, Shale oil cracking kinetics and diagnostics, Ind. Eng. Chem. Process Des. Dev. 24 (1985) 381–386.
[3] F. Sefidvash, Status of the small modular fluidized bed lightwater nuclear reactor concept, Nucl. Eng. Des. 167 (1996) 203.
[4] S. Shyuer-Ming, P.D. Komar, Sediments, beach morphology and sea cliff erosion within an Oregon Coastal littoral cell, J. Coast. Res. 10 (1994) 144–157.
[5] P.M. Holton, D.L. Tackett, K. Willeke, Particle size-dependent leakage and losses of aerosols in respirators, Am. Ind. Hyg. Assoc. J. 48 (1987) 848–854.
[6] A. Hölzer, M. Sommerfeld, New simple correlation formula for the drag coefficient of non-spherical particles, Powder Technol. 184 (2008) 361–365.
[7] M. Moreau, O. Simonin, B. Bédat, Development of gas-particle Euler–Euler LES approach: A priori analysis of particle sub-grid models in homogeneous isotropic turbulence, Flow Turbul. Combust. 84 (2009) 295–324.
[8] O.A. Druzhinina, S. Elghobashi, On the decay rate of isotropic turbulence laden with microparticles, Phys. Fluids 11 (1999) 602–611.
[9] D. Squires, J.K. Eaton, Particle response and turbulence modification in isotropic turbulence, Phys. Fluids 2 (1990) 1191–1204.
[10] C. Corre, J.-L. Estivalezes, S. Vincent, O. Simonin, S. Glockner, Simulation of a fluidized bed using a hybrid Eulerian–Lagrangian method for particle tracking, Notes Numer. Fluid Mech. Multidiscipl. Des. 110 (2010) 103–110.
[11] A. Ferrante, S. Elghobashi, On the physical mechanisms of two-way coupling in particle-laden isotropic turbulence, Phys. Fluids 15 (2003) 315–329.
[12] A.M. Ahmed, S. Elghobashi, Direct numerical simulation of particle dispersion in homogeneous turbulent shear flows, Phys. Fluids 13 (2001) 3346–3364.
[13] P. Fede, O. Simonin, Numerical study of the subgrid fluid turbulence effects on the statistics of heavy colliding particles, Phys. Fluids 18 (2006) 045103–045120.
[14] H.H. Hu, D.D. Joseph, M.J. Crochet, Direct simulation of fluid particle motions, Theor. Comput. Fluid Mech. 3 (1992) 285–306.
[15] E.A. Fadlun, R. Verzicco, P. Orlandi, J. Mohd-Yusofz, Combined immersed-boundary finite-difference methods for three-dimensional complex flow simulations, J. Comput. Phys. 161 (2000) 35–60.
[16] J. Kim, D. Kim, H. Choi, An immersed-boundary finite-volume method for simulations of flow in complex geometries, J. Comput. Phys. 171 (2001) 132–150.
[17] S. Takagi, H.N. Oğuz, Z. Zhang, A. Prosperetti, PHYSALIS: A new method for particle simulation: Part II: Two-dimensional Navier–Stokes flow around cylinders, J. Comput. Phys. 187 (2003) 371–390.
[18] M. Coquerelle, G.H. Cottet, A vortex level set method for the two-way coupling of an incompressible fluid with colliding rigid bodies, J. Comput. Phys. 227 (2008) 9121–9137.
[19] J.A. Simeonov, J. Calantoni, A pressure boundary integral method for direct fluid–particle simulations on Cartesian grids, J. Comput. Phys. 230 (2011) 1749–1765.
[20] K. Höfler, S. Schwarzer, Navier–Stokes simulation with constraint forces: Finite-difference method for particle-laden flows and complex geometries, Phys. Rev. E 61 (2000) 7146–7160.
[21] B. Maury, Direct simulations of 2D fluid–particle flows in biperiodic domains, J. Comput. Phys. 156 (1999) 325–351.
[22] S.H. Cho, H.G. Choi, J.Y. Yoo, Direct numerical simulation of fluid flow laden with many particles, Int. J. Multiph. Flow 31 (2005) 435–451.
[23] H.H. Hu, N.A. Patankar, M.Y. Zhu, Direct numerical simulations of fluid–solid systems using the arbitrary Lagrangian–Eulerian technique, J. Comput. Phys. 169 (2001) 427–462.
[24] R. Glowinski, T.W. Pan, T.I. Hesla, D.D. Joseph, J. Périaux, A fictitious domain approach to the direct numerical simulation of incompressible viscous flow past moving rigid bodies: Application to particulate flow, J. Comput. Phys. 169 (2001) 363–426.
[25] Z. Zhang, A. Prosperetti, A second-order method for three-dimensional particle simulation, J. Comput. Phys. 210 (2005) 292–324.

[26] M. Uhlmann, An immersed boundary method with direct forcing for the simulation of particulate flows, J. Comput. Phys. 209 (2) (2005) 448–476.
[27] M. Uhlmann, Interface-resolved direct numerical simulation of vertical particulate channel flow in the turbulent regime, Phys. Fluids 20 (5) (2008) 053305.
[28] A. Ten Cate, J.J. Derksen, L.M. Portela, E.A. Van Der Akker, Fully resolved simulations of colliding monodisperse spheres in forced isotropic turbulence, J. Fluid Mech. 519 (2004) 233–271.
[29] H. Gao, L.-P. Wang, Lattice Boltzmann simulation of turbulent flow laden with finite-size particles, in: Proceedings of the 7th International Conference on Multiphase Flows ICMF 2010, 2010.
[30] F. Lucci, A. Ferrante, S. Elghobashi, Modulation of isotropic turbulence by particles of Taylor length-scale size, J. Fluid Mech. 650 (2010) 5–55.
[31] F. Lucci, A. Ferrante, S. Elghobashi, Is Stokes number an appropriate indicator for turbulence modulation by particles of Taylor-length-scale size?, Phys. Fluids 23 (2011) 025101.
[32] J.-B. Ritz, J.P. Caltagirone, A numerical continuous model for the hydrodynamics of fluid particle systems, Int. J. Numer. Methods Fluids 30 (1999) 1067–1090.
[33] T.N. Randrianarivelo, G. Pianet, S. Vincent, J.-P. Caltagirone, Numerical modelling of the solid particle motion using a new penalty method, Int. J. Numer. Methods Fluids 47 (2005) 1245–1251.
[34] T.N. Randrianarivelo, S. Vincent, O. Simonin, J.-P. Caltagirone, A DNS approach dedicated to the analysis of fluidized beds, Fluid Mech. Appl. 81 (2007) 207–214.
[35] T.W. Pan, D.D. Joseph, R. Bai, R. Glowinski, V. Sarin, Fluidization of 1204 spheres: Simulation and experiment, J. Fluid Mech. 451 (2002) 169–191.
[36] C. Peskin, The immersed boundary method, Acta Numer. 11 (2002) 1–39.
[37] G. Pianet, A. Ten Cate, J.J. Derksen, E. Arquis, Assessment of the 1-fluid method for DNS of particulate flows: Sedimentation of a single sphere at moderate to high Reynolds numbers, Comput. Fluids 36 (2007) 359–375.
[38] S. Vincent, J.-P. Caltagirone, P. Lubin, N. Randrianarivelo, An adaptative augmented Lagrangian method for three-dimensional multi-material flows, Comput. Fluids 33 (2004) 1273–1289.
[39] S. Vincent, T. Randrianarivelo, G. Pianet, J.P. Caltagirone, Local penalty methods for flows interacting with moving solids at high Reynolds numbers, Comput. Fluids 36 (2007) 902–913.
[40] J.C. Brändle De Motta, S. Vincent, J.-L. Estivalezes, E. Climent, Fictitious domain methods and penalty techniques for the simulation of turbulent particulate flows, in: ASME Fluid Summer Meeting, Montreal, August 4–7, 2010.
[41] I. Kataoka, Local instant formulation of two-phase flow, Int. J. Multiph. Flow 12 (1986) 745–758.
[42] C. Dobrzynski, P. Frey, Anisotropic Delaunay mesh adaptation for unsteady simulations, in: Proceedings of the 17th International Meshing Roundtable, 2008.
[43] K. Khadra, Ph. Angot, S. Parneix, J.P. Caltagirone, Fictitious domain approach for numerical modelling of Navier–Stokes equations, Int. J. Numer. Methods Fluids 34 (2000) 651–684.
[44] J.M. Delahye, Jump conditions and entropy sources in two-phase systems. Local instant formulation, Int. J. Multiph. Flow 1 (1974) 395–409.
[45] I. Kataoka, M. Ishii, A. Serizawa, Local formulation and measurements of interfacial area concentration in two-phase flow, Int. J. Multiph. Flow 12 (July–August 1986) 505–529.
[46] R. Scardovelli, S. Zaleski, Direct numerical simulation of free-surface and interfacial flow, Annu. Rev. Fluid Mech. 31 (1999) 567–603.
[47] P. Sagaut, Large Eddy Simulation for Incompressible Flows – An Introduction, Springer Verlag, 1998.
[48] S. Vincent, D. Lacanette, J. Larocque, A. Toutant, P. Lubin, P. Sagaut, Direct numerical simulation of phase separation and a priori two-phase LES filtering, Comput. Fluids 37 (2008) 898–906.
[49] I. Ryhming, Dynamique des Fluides, Presses Polytechniques Romanes, 1985.
[50] J. Happel, H. Brenner, Low Reynolds Number Hydrodynamics, Kluwer Academic Publishers, 1963.
[51] J.-P. Caltagirone, S. Vincent, Tensorial penalisation method for solving Navier–Stokes equations, C. R. Acad. Sci., Sér. 2b 329 (2001) 607–613.
[52] M. Fortin, R. Glowinski, Méthodes de lagrangien augmenté. Application à la résolution numérique de problèmes aux limites, Dunod, Paris, 1982.
[53] S. Vincent, A. Sarthou, J.-P. Caltagirone, F. Sonilhac, P. Février, C. Mignot, G. Pianet, Augmented Lagrangian and penalty methods for the simulation of two-phase flows interacting with moving solids. Application to hydroplaning flows interacting with real tire tread patterns, J. Comput. Phys. 230 (2011) 956–983.
[54] A. Benkenida, J. Magnaudet, A method for the simulation of two-phase flows without interface reconstruction, C. R. Acad. Sci., Sér. 2b, Méc. Fluids 328 (2000) 25–32.
[55] C.W. Hirt, A.A. Amsden, J.L. Cook, An arbitrary Lagrangian–Eulerian computing method for all flow speeds, J. Comput. Phys. 14 (1974) 227–253.
[56] D.L. Youngs, Time-dependent multimaterial flow with large fluid distortion, in: K.W. Morton, M.J. Baines (Eds.), Numerical Methods for Fluid Dynamics, Academic, New York, 1982.
[57] R.M. Cabezón, D. García-Senz, A. Relaño, A one-parameter family of interpolating kernels for smoothed particle hydrodynamics studies, J. Comput. Phys. 227 (2008) 8523–8540.
[58] G.C. Truesdell, S.E. Elghobashi, On the two-way interaction between homogeneous turbulence and dispersed solid particles; Part 2: Particle dispersion, Phys. Fluids 6 (1994) 1405–1407.
[59] C. Poelma, J. Westerweel, G. Ooms, Particle–fluid interactions in grid-generated turbulence, J. Fluid Mech. 589 (2007) 315–351.
[60] A. Lefebvre, Numerical modeling of fluid/particle flows. Accounting of lubrication effects, PhD thesis, Paris-Sud. Faculté des Sciences d'Orsay, 2007.
[61] A.M. Ardekani, R.H. Rangel, Numerical investigation of particle–particle and particle–wall collisions in a viscous fluid, J. Fluid Mech. 596 (2008) 437–466.
[62] W.-P. Breugem, A combined soft-sphere collision/immersed boundary method for resolved simulations of particulate flows, in: Proceedings of the ASME 2010 3rd Joint US–European Fluids Engineering Summer Meeting and 8th Interational Conference on Nanochannels, Microchannels, and Minichannels, FEDSM2010–ICNMM2010, Montreal, Quebec, Canada, 1–5 August, 2010, Paper number FEDSM-ICNMM2010-30634.
[63] C.T. Crowe, M. Sommerfeld, Y. Tsuji, Multiphase Flows with Droplets and Particles, CRC, 1998.
[64] J.C. Brändle de Motta, W.P. Breugem, B. Gazanion, J.-L. Estivalezes, S. Vincent, E. Climent, Numerical modelling of finite-size particle collisions in a viscous fluid, Phys. Fluids 25 (2013) 083302.
[65] B. Maury, A many-body lubrication model, C. R. Acad. Sci., Sér. 1 Math. 325 (1997) 1053–1058.
[66] S.L. Dance, M.R. Maxey, Incorporation of lubrication effects into the force-coupling method for particulate two-phase flow, J. Comput. Phys. 189 (1) (2003) 212–238.
[67] H. Brenner, The slow motion of a sphere through a viscous fluid towards a plane surface, Chem. Eng. Sci. 16 (3–4) (1961) 242–251.
[68] S.E. Elghobashi, On predicting particle-laden turbulent flows, Appl. Sci. Res. 52 (1994) 309–329.
[69] S. Laín, M. Sommerfeld, J. Kussin, Experimental studies and modelling of four-way coupling in particle-laden horizontal channel flow, Int. J. Heat Fluid Flow 23 (2002) 647–656.
[70] D. Legendre, C. Daniel, P. Guiraud, Experimental study of a drop bouncing on a wall in a liquid, Phys. Fluids 17 (2005) 097105.
[71] A. Poux, S. Glockner, M. Azaïez, Improvements on open and traction boundary conditions for Navier–Stokes time-splitting methods, J. Comput. Phys. 230 (2011) 4011–4027.

[72] F. Bertrand, P.A. Tanguy, F. Thibault, A three-dimensional fictitious domain method for incompressible fluid flow problems, Int. J. Numer. Methods Fluids 25 (1997) 719–736.
[73] O. Schenk, K. Gärtner, Solving unsymmetric sparse systems of linear equations with PARDISO, Future Gener. Comput. Syst. 20 (2004) 475–487.
[74] I. Gustafsson, On First- and Second-Order Symmetric Factorisation Methods for the Solution of Elliptic Difference Equations, Chalmers University of Technology, 1978.
[75] R.H.A. Van Der Vorst, BiCGSTAB: A fast and smoothly converging variant of BiCG for the solution of non-symmetric linear systems, SIAM J. Sci. Stat. Comput. 13 (1992) 631–644.
[76] E. Ahusborde, S. Glockner, An implicit method for the Navier–Stokes equations on overlapping block-structured grids, Int. J. Numer. Methods Fluids 62 (2010) 784–801.
[77] B.J. Alder, T.E. Wainwright, Studies in molecular dynamics. I. General method, J. Chem. Phys. 31 (1959) 459.
[78] B.J. Alder, T.E. Wainwright, Studies in molecular dynamics. II. Behavior of a small number of elastic spheres, J. Chem. Phys. 33 (1960) 1439.
[79] L. Verlet, Computer "Experiments" on classical fluids. I. Thermodynamical properties of Lennard-Jones molecules, Phys. Rev. 159 (1) (1967) 98.
[80] X. Fang, J. Tang, H. Luo, Granular damping analysis using an improved discrete element approach, J. Sound Vib. 308 (1–2) (2007) 112–131.
[81] L.F. Richardson, J.A. Gaunt, The deferred approach to the limit, Philos. Trans. R. Soc. Lond. Ser. A, Math. Phys. Sci. 226 (1927) 299–361.
[82] A. Ten Cate, C.H. Nieuwstad, J.J. Derksen, H.E.A. Van den Akker, Particle imaging velocimetry experiments and lattice-Boltzmann simulations on a single sphere settling under gravity, Phys. Fluids 14 (2002) 4012–4025.
[83] S.V. Apte, M. Martin, N.A. Patankar, A numerical method for fully resolved simulation (FRS) of rigid particle–flow interactions in complex flows, J. Comput. Phys. 228 (2009) 2712–2738.
[84] T. Kempe, J. Fröhlich, On Euler–Lagrange coupling and collision modelling for spherical particles, in: 8th International ERCOFTAC Symposium on Engineering Turbulence Modelling and Measurements, Marseille, France, 2010.
[85] G.G. Stokes, On the theories of the internal friction of fluids in motion, and of the equilibrium and motion of elastic solids, Trans. Camb. Philos. Soc. 8 (1845) 287.
[86] H. Lamb, Hydrodynamics, Cambridge University Press, 1932.
[87] C.R. Dennis, S.N. Singh, D.B. Ingham, The steady flow due to a rotating sphere at low and moderate Reynolds numbers, J. Fluid Mech. 101 (1980) 257–279.
[88] O. Sawatzki, Das Strömungsfeld um eine rotierende Kugel, Acta Mech. 9 (1970) 159–214.
[89] E. Climent, K. Yeo, M.R. Maxey, G.E. Karniadakis, Dynamic self-assembly of spinning particles, J. Fluids Eng. 129 (2007) 379–387.
[90] W.H.H. Banks, The boundary layer on a rotating sphere, Q. J. Mech. Appl. Math. 18 (1965) 443–454.
[91] G. Segre, A. Silberberg, Radial particle displacements in Poiseuille flow of suspensions, Nature 189 (1961) 209–210.
[92] G. Segré, A. Silberberg, Behaviour of macroscopic rigid spheres in Poiseuille flow. Part 1. Determination of local concentration by statistical analysis of particle passages through crossed light beams, J. Fluid Mech. 14 (1962) 115–135.
[93] G. Segré, A. Silberberg, Behaviour of macroscopic rigid spheres in Poiseuille flow. Part 2. Experimental results and interpretation, J. Fluid Mech. Digit. Arch. 14 (1962) 136–157.
[94] M. Tachibana, On the behaviour of a sphere in the laminar tube flows, Rheol. Acta 12 (1973) 58–69.
[95] J.-P. Matas, J.F. Morris, E. Guazzelli, Inertial migration of rigid spherical particles in Poiseuille flow, J. Fluid Mech. 515 (2004) 171–195.
[96] D.H. Douglas-Hamilton, N.G. Smith, C.E. Kuster, J. Vermeiden, G.C. Althouse, Capillary-loaded particle fluid dynamics: effect on estimation of sperm concentration, J. Androl. 26 (2005) 115.
[97] A. Karnis, H.L. Goldsmith, S.G. Mason, The flow of suspensions though tubes. V: Inertial effects, Can. J. Chem. Eng. (1966).
[98] M. Han, C. Kim, M. Kim, S. Lee, Particle migration in tube flow of suspensions, J. Rheol. 43 (1999) 1157.
[99] Takaji Inamuro, Koji Maeba, Fumimaru Ogino, Flow between parallel walls containing the lines of neutrally buoyant circular cylinders, Int. J. Multiph. Flow 26 (2000) 1981–2004.
[100] T.-W. Pan, R. Glowinski, Direct simulation of the motion of neutrally buoyant circular cylinders in plane Poiseuille flow, J. Comput. Phys. 181 (2002) 260–279.
[101] J.F. Richardson, W.N. Zaki, Sedimentation and fluidization. Part 1, Chem. Eng. Res. Des. 32 (1954) 35–53.
[102] O. Simonin, P.L. Viollet, Modelling of turbulent two-phase jets loaded with discrete particles, Phase-Interface Phenom. Multiph. Flow (1990) 259–269.
[103] M. Boivin, O. Simonin, K.D. Squires, Direct numerical simulation of turbulence modulation by particles in isotropic turbulence, J. Fluid Mech. 375 (1998) 235–263.
[104] J.J. Derksen, S. Sundaresan, Direct numerical simulations of dense suspensions: Wave instabilities in liquid-fluidized beds, J. Fluid Mech. 587 (2007) 303–336.
[105] A. Aguilar Corona, Agitation of particles in a liquid fluidized bed. Experimental study, PhD thesis, Toulouse University, 2008.
[106] A.S. Sangani, G. Mo, H.K. Tsao, D.L. Koch, Simple shear flows of dense gas–solid suspensions at finite Stokes numbers, J. Fluid Mech. 313 (1996) 309–341.
[107] M. Abbas, E. Climent, J.-F. Parmentier, O. Simonin, Flow of particles suspended in a sheared viscous fluid: Effects of finite inertia and inelastic collisions, AIChE J. 56 (2008) 2523–2538.